Solidification and Cooling Analysis of Aluminum Alloy Droplets with the Uniform Droplet Spray Process

by

Jean-Pei Jeanie Cherng

S.B. Mechanical Engineering, 1995
Massachusetts Institute of Technology

Submitted to the Department of Mechanical Engineering
in Partial Fulfillment of the Requirements for the Degree of

MASTER OF SCIENCE IN MECHANICAL ENGINEERING
at the
MASSACHUSETTS INSTITUTE OF TECHNOLOGY

February 1997

Signature of Author: _____
Department of Mechanical Engineering
January 17, 1997

Certified by: _____
Dr. Jung-Hoon Chun
Edgerton Associate Professor of Mechanical Engineering
Thesis Supervisor

Accepted by: _____
Dr. Ain A. Sonin
Professor of Mechanical Engineering
Chairman, Department Graduate Committee

Solidification and Cooling Analysis of Aluminum Alloy Droplets with the Uniform Droplet Spray Process

by

Jean-Pei Jeanie Cherng

Submitted to the Department of Mechanical Engineering
on January 17, 1997 in Partial Fulfillment of the Requirements for the Degree of
Master of Science in Mechanical Engineering

ABSTRACT

The uniform droplet spray (UDS) process is a process in which uniformly-sized, molten metal droplets are created and sprayed onto a substrate to form a bulk deposit. The UDS process has been successful in producing fully dense deposits of fine equiaxed microstructure from tin alloys. There is growing interest to apply the UDS process to higher-melting-temperature alloys such as aluminum alloys for the rapid production of near-net-shaped parts.

Because of the high affinity of liquid aluminum to oxygen, an oxygen-reducing environment was developed to produce uniform droplet sprays of aluminum alloys. In the spray chamber below 1 ppm of oxygen, the sprays were obtained from 150 and 200 μm diameter orifices with mass flow rates of approximately 0.25 and 0.43 g/sec, respectively.

The quality of a sprayed deposit in terms of microstructure and bulk porosity depends on the thermal state of the incoming droplets as they impact the top surface of the deposit. To predict the temperature and solid fraction of the droplet as a function of flight distance, a droplet thermal model was developed by assuming Newtonian cooling and employing the Scheil equation and a droplet trajectory model. The droplet thermal model was experimentally tested by quenching droplets of Al-4.5wt% Cu and Al-4.3wt% Fe alloys at different flight distances. The volume fraction of solid in the droplets prior to quenching was measured to verify the droplet thermal model.

The evolution of microstructure during solidification was observed in quenched droplets of Al-4.5wt% Cu about 295 μm in diameter. Secondary dendrite arm spacing of the powder microstructure agrees with the cooling rate predicted by the droplet thermal model within an order of magnitude. However, the measured values of solid fraction appear to be inflated due to a mushy zone from the solid solubility of copper in aluminum. The solidification behavior of the 250 μm droplets of Al-4.3wt% Fe exhibited completely undercooled droplets within 0.5 m of flight, thereby causing the equilibrium solidification model to be inapplicable. Recommendations for future work are made.

Thesis Supervisor:

Dr. Jung-Hoon Chun
Esther and Harold E. Edgerton Associate Professor of Mechanical Engineering

Acknowledgments

First and foremost, I would like to thank my advisor, Professor Jung-Hoon Chun, for giving me the opportunity to work on this project. His support, guidance, and patience during the past two years are always much appreciated.

I am also grateful to Professor Teiichi Ando at Northeastern University and Dr. Men Chu at the Aluminum Company of America who generously provided their expertise in materials science. Sincere thanks to Dr. Craig Blue at the Oak Ridge National Laboratory for sharing his design ideas and experiences with me. More thanks to Dr. Chu and Dr. Blue for supplying the aluminum alloy material for my experiments. And many thanks to Dr. Nannaji Saka for being a nice critic of my research.

I would also like to thank all the friends in the Droplet Based Manufacturing Laboratory at MIT for being so pleasant to work with day after day. Special thanks to Dr. Chen-An Chen for guiding me through my research with his deep knowledge on the subject. Without his wise advice, my accomplishments would not have been possible. Thanks to Dr. Pyongwon Yim for teaching me how to be resourceful in my experiments and realistic in life. Thanks to Sukyoung Chey for helping to fix my mistakes. Thanks to Ho-Young Kim for keeping me awake during those endless nights in lab. Thank you, Juan-Carlos Rocha and Jiun-Yu Lai, for giving me space to do my experiments and helping me in lab.

I would also like to thank other lab members: Jim Derksen, Sangjun Han, Mark Hytros, and Dongsik Kim. Thank you to Yin Lin Xie and Nil Chatterjee for their help with the metallographic work. And sincere gratitude to Fred Cote and Wes Williams for showing me the art of machining.

Having stayed at MIT for a number of years and looking forward to the years to come, I owe my sanity to many special friends. Thanks to Terence Chow, Alexandra Hou, Alice Lin, Nancy Xiao, and Clara Yang. Most significantly, I would like to thank Hector Ayala for his friendship and consideration, and not to mention his Powerbook Duo with which this thesis was written.

Last but not least, I am truly blessed with my loving parents and sisters. Thank you, Mom and Dad, Chi-Pei, Mary, Rae, and Wendy, for your unconditional love and support. I love you all very much.

Table of Contents

List of Figures

List of Tables

Chapter 1 INTRODUCTION

1.1 Background

Spray forming is a metal droplet deposition process that produces near-net-shaped preforms directly from molten metal alloys. In a single operation, a liquid metal stream is atomized into fine droplets by high-pressure inert gas and sprayed onto a motion-controlled substrate on which the droplets consolidate to form a bulk deposit. Large-diameter tubes and cylindrical billets are the most common shapes for spray-deposited preforms [Leatham 1996]. Figure 1.1 shows a schematic of the spray forming process. Spray forming is an attractive alternative to conventional ingot metallurgy processes that involve multiple steps such as ingot casting, forging, and/or rolling, and to powder metallurgy methods of particulate consolidation. Rapid solidification of the droplets upon deposition enhances the mechanical properties of spray-formed products without requiring extensive secondary processing. Their microstructures exhibit refined grain sizes, reduced phase segregation, and increased solubility of alloying elements. Furthermore, spray forming has the potential to lower capital costs (less equipment required), lower operating costs (low energy consumption and high material yields), and lower overhead costs (less stock and work-in progress time). [Leatham 1996]

Since its invention in the early 1970s, however, spray forming has yet to fully present itself as a commercially viable process in industry. In order to retain a competitive advantage at high volume production-scale, spray-formed products must meet critical requirements of high yield, fine grain size, low porosity, and microstructural uniformity. Yield losses associated with material overspray may currently be as high as 20% to 30% [Tyler and Watson 1996]. Overspray is made up of droplets which miss the deposition surface or splash off due to high liquid fraction and high velocity gas impingement [Mathur et al 1991]. Overspray is particularly a concern when producing strips or sheet products. Conventional spray forming through circular gas atomizers is limited to producing conical sprays with a Gaussian distribution of droplet flux. Thus, sprayed deposits are thicker in the center and thinner at the circumference. Scanning atomizers which attempt to evenly distribute the molten metal spray by swiveling or scanning suffer from high overspray. Several linear nozzle configurations have been developed to overcome this problem for improved flatness of wide sheets as well as to increase production rate [Tsao and Grant 1994, Leon and Kozarek 1995].

Another significant problem in conventional spray forming is porosity. The volume fraction of porosity in sprayed products has been shown to range from 1% to 7% which

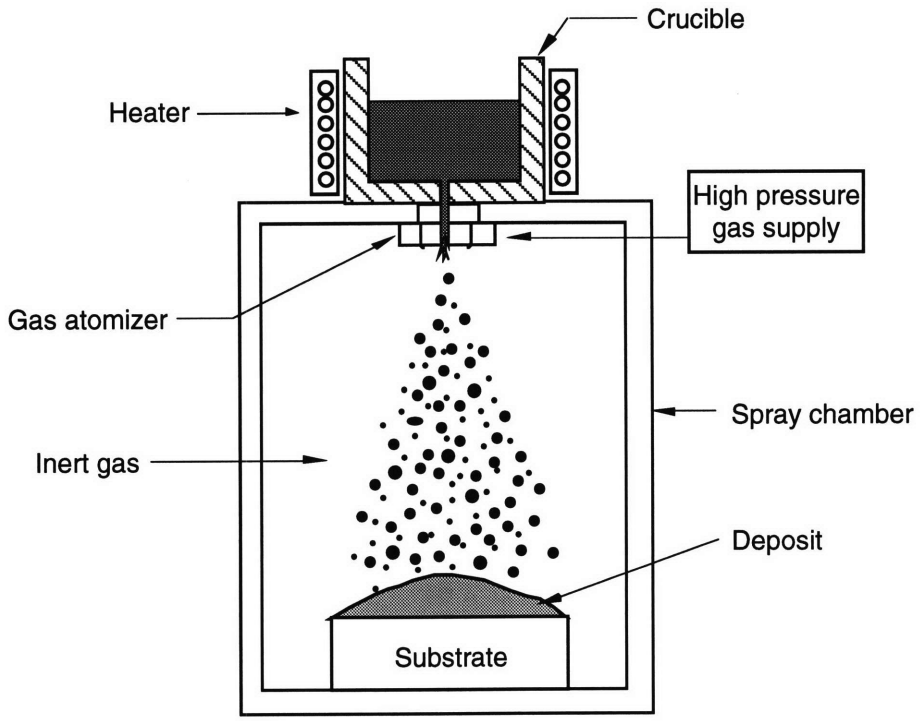

Figure 1.1 Schematic diagram of a conventional spray forming process.

must be reduced through subsequent thermo-mechanical processing [Tsao and Grant 1994, Underhill et al 1993]. Porosity is caused by non-optimal solid fraction in the spray upon impact on the substrate. When the volume fraction of solid deposited at the surface is too low, turbulent interactions between the atomizing gas and liquid deposit surface may lead to pores of entrapped gas in the final product. However, when the solid fraction is too high, on the other hand, insufficient molten material may be available to fill the interstices between splats, resulting in a porous deposit [Grant and Cantor 1995, Lee and Ahn 1994, Annavarapu and Doherty 1993].

To control the microstructure and reduce porosity levels in the final deposit, therefore, it is necessary to understand the thermal states of the droplets in flight. In gas-atomized spray forming, the spray contains a wide distribution of droplet diameters. The differently sized droplets will have different velocities and will solidify at different rates. The smaller droplets will tend to have higher solid fraction than the larger ones at impact. This inherent variation of the droplet solid fraction in gas atomized sprays restricts the degree of attainable microstructures and droplet consolidation.

The uniform droplet spray (UDS) process was developed to overcome the shortcomings of conventional spray forming [Passow 1992]. The UDS process produces a spray of molten metal droplets that are uniform in size. Based on Rayleigh's capillarity

instability of a laminar jet, a jet of molten metal is broken into uniform droplets by applying a periodic perturbation to the jet at a specific frequency and amplitude. The droplets are electrically charged to the same polarity to prevent in-flight merging. As a result of the uniform droplet size distribution, the dynamic and thermal states of the droplets can be precisely controlled in the UDS process. Given these inputs, the microstructure of the sprayed deposit can be tailored for optimal mechanical behavior. The UDS process also has the ability to spray a uniform distribution profile and reduce yield loss by manipulating a multi-nozzle configuration [Abel 1994].

The UDS process has been successfully used to spray uniform droplets of tin, tin-lead alloys, zinc alloys, and waxy and polymeric materials with diameters ranging from 50 to 800 μm. Its potential applications include near-net-shape fabrication of metallic parts, rapid prototyping, and the production of uniform powders for electronics packaging as well as sintered filters. Fully dense deposits with distinct microstructures, such as fine equiaxed grains or epitaxial columnar grains, have been produced from tin-lead alloys [Chen et al 1996]. Application of the UDS process to higher-melting-point materials such as aluminum alloys is the next stage of development.

1.2 Motivation and Goals of Research

In aerospace and automotive industries where weight savings are critical for fuel efficiency, there has been increasing interest in using spray forming to promote microstructural refinement and improve mechanical behavior in structural aluminum alloys [Lavernia et al 1992]. For example, the production of continuous aluminum sheets directly from the melt has received much attention [Leon and Kozarek 1995]. Aluminum sheet products are conventionally manufactured by direct chill casting a slab that is typically 300 mm thick. The slab undergoes energy-intensive scalping and homogenization steps to break down its coarse dendritic grain structure and large scale phase segregation. The slab is then progressively rolled to its final sheet thickness of about 5 mm [Chu 1996]. Although spray forming advocates are developing methods to produce high quality aluminum sheet products directly from the melt, their efforts have been hindered by the previously mentioned problems of overspray, porosity formation, and non-uniform microstructure.

Therefore, the goal of this research is to extend the UDS process capability to spraying aluminum alloys for the rapid production of near-net-shaped parts. To achieve fully dense deposits with fine equiaxed microstructures, it is essential to have control over the droplet thermal states during flight. Thus, the objectives are to develop a numerical model to predict the solidification and cooling behavior of aluminum alloy droplets, and to

experimentally verify the model with uniform droplets of Al-4.5wt% Cu and Al-4.3wt% Fe alloys.

Application of the UDS process to aluminum alloys poses a significant challenge. The oxidation of a liquid metal jet has been shown to hinder uniform jet break-up. In the open air, a jet of pure tin will solidify as a beaded wire instead of breaking into droplets [Passow 1992]. Yim [1996] established that the threshold level for uniform break-up of tin-lead alloys is 1500 ppm of oxygen. Aluminum is more reactive to oxygen than tin. However, no previous work has been made towards understanding the behavior of molten aluminum in the UDS process.

1.3 Outline of Study

This chapter provides an introduction to the project, its primary objectives and a brief look at the motivation behind the application of the UDS process to aluminum alloys. Chapter 2 describes the how the UDS apparatus and procedure were adapted for a higher-melting-point material with a stronger affinity to oxygen than tin or zinc alloys. After successfully producing uniform droplet sprays of aluminum alloy, Chapter 3 presents the physical models of jet break-up, droplet trajectory, droplet heat transfer, and droplet solidification. Chapter 4 describes the experimental method employed to verify the droplet solidification model by measuring the droplet solid fraction at different flight distances. The results obtained are compared with the simulation results and discussed. A summary of the thesis and recommendations for future work are given in Chapter 5.

Chapter 2 EXPERIMENTAL APPARATUS AND PROCEDURE

A schematic of the UDS apparatus is shown in Figure 2.1. It consists of a droplet generator unit, a glass-column spray chamber, a regulated inert gas supply system, a vacuum pump, and a video monitoring system. The droplet generator unit is mounted on top of the glass chamber; the entire system is vacuumed and then filled with inert gas.

A schematic of a low-temperature droplet generator unit is shown in Figure 2.2. It was designed to spray low-melting-point (less than 500°C) materials such as tin and zinc alloys. The metal is melted in a stainless-steel crucible with an electrical band heater. In the crucible bottom, a stainless steel mesh screen and an orifice are placed. When the crucible is pressurized by inert gas, typically between 30 and 200 kPa, a laminar stream of molten metal exits through the orifice. The stream breaks up into uniform droplets when vibrations are imposed on the exiting jet by a shaft driven by a stack of piezoelectric transducers at a specified frequency. The break-up frequency which ranges from 1 to 25 kHz is determined by the jet diameter and jet velocity as discussed later in Chapter 3. A DC-voltage charging ring is placed at the point of jet break-up such that the droplets become electrically charged to the same polarity to prevent them from merging into each other. The mutual repulsion between the droplets cause them to scatter and form a spray cone. By varying the charging voltage between 400 and 3000 V, the mass flux distribution can be controlled. The droplets are deposited onto a motion- and temperature-controlled substrate to produce the desired geometry and microstructure.

The video monitoring system allows for observation of jet break-up by using a CCD camera (Techni-Quip #TQ-VA), a synchronized strobe light (Pioneer #DS-303), and a monitor (Sony #PVM-1390). A function generator (BK Precision #3011B) connected to an power amplifier (Radio Shack #MAP-30) and transformer produces a square wave voltage signal which drives the piezoelectric transducers (Morgan Matroc #PZT-5A). The voltage applied to the charging ring is supplied by a high DC voltage source (Bertran #230). The temperature of the melt is controlled with a K-type thermocouple and a solid-state temperature controller (OMEGA #CN9500). The gas regulators control the gas pressure in the crucible and the chamber independently to establish a positive pressure differential in the crucible.

A droplet generator capable of handling 1100°C was designed and built as shown in Figure 2.3 [Abel 1993]. The major difference between the high- and low-temperature generators is the heater design. The high-temperature unit has a separate furnace section

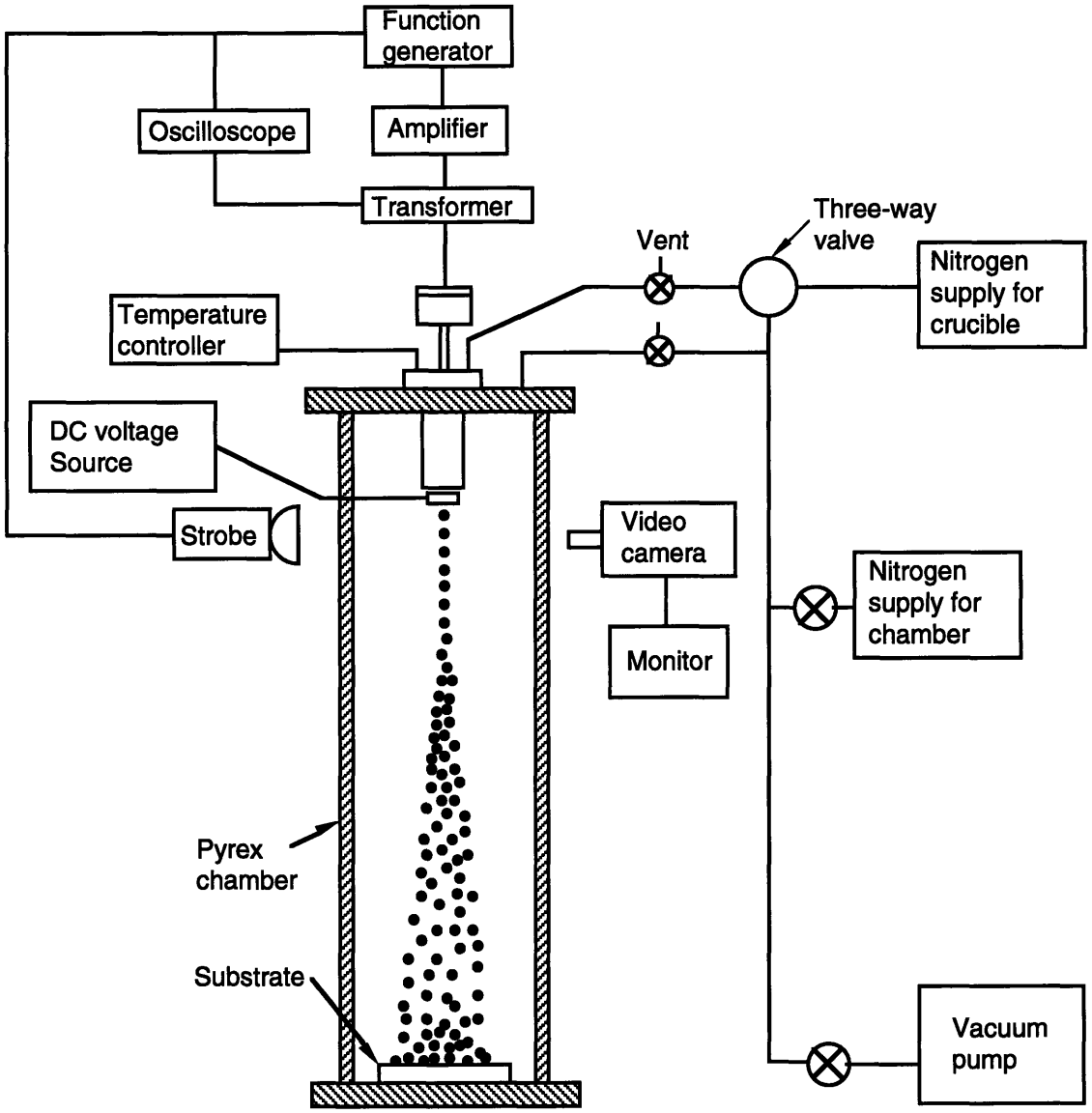

Figure 2.1 Schematic diagram of the UDS apparatus.

which contains an electric clamshell heater (Mellen #1SKE-203-071) and fiber insulation. The two-part graphite crucible is assembled separately on the top plate and then placed into the furnace section. Two viewports were added to the furnace section to observe jet break-up below the crucible [Williams 1996]. The charging ring was also moved so that it is not attached to the bottom of the graphite crucible. This was done to provide a sufficient dielectric gap between the charging ring and the crucible at high temperatures. Although the droplet generator reached adequate operating temperature, preliminary attempts to establish the uniform break-up of aluminum alloys were not successful.

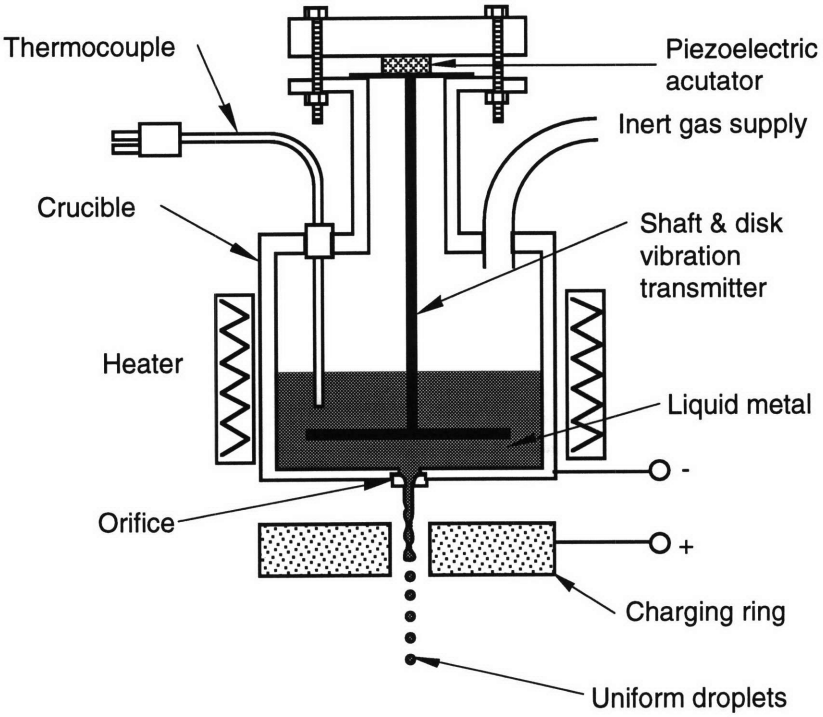

Figure 2.2 Schematic diagram of the low-temperature droplet generator.

2.1 Challenges in Spraying Aluminum Alloys

Initial attempts to spray pure aluminum with a 100 μm orifice produced erratic stream behaviors when the same operating procedures as those developed for spraying tin or zinc alloys were used. The jet of molten aluminum wandered back and forth from a vertically stable position causing the jet break-up to be unsteady. Sometimes no melt would exit. Sometimes the jet would exit, but begin to thin, and then drip until completely stopped. This stream behavior had not been previously experienced with any other material. The problem was attributed to the oxide formation in the crucible.

It is well-known that aluminum and its alloys readily oxidize. Nylund et al [1991] analyzed the surface of gas-atomized Al-alloy powders that were produced, handled, and stored in an inert gas atmosphere with oxygen partial pressure ranging from 20 to 50 ppm. Using Auger spectroscopy, it was determined that during atomization, discrete oxide islands 50 Å in depth, are formed on the particle surfaces. The formation of surface oxide is controlled by the availability of reactants in the liquid metal and gas phases as well as the transportation of oxygen to the liquid metal surface. The standard Gibbs free energy of

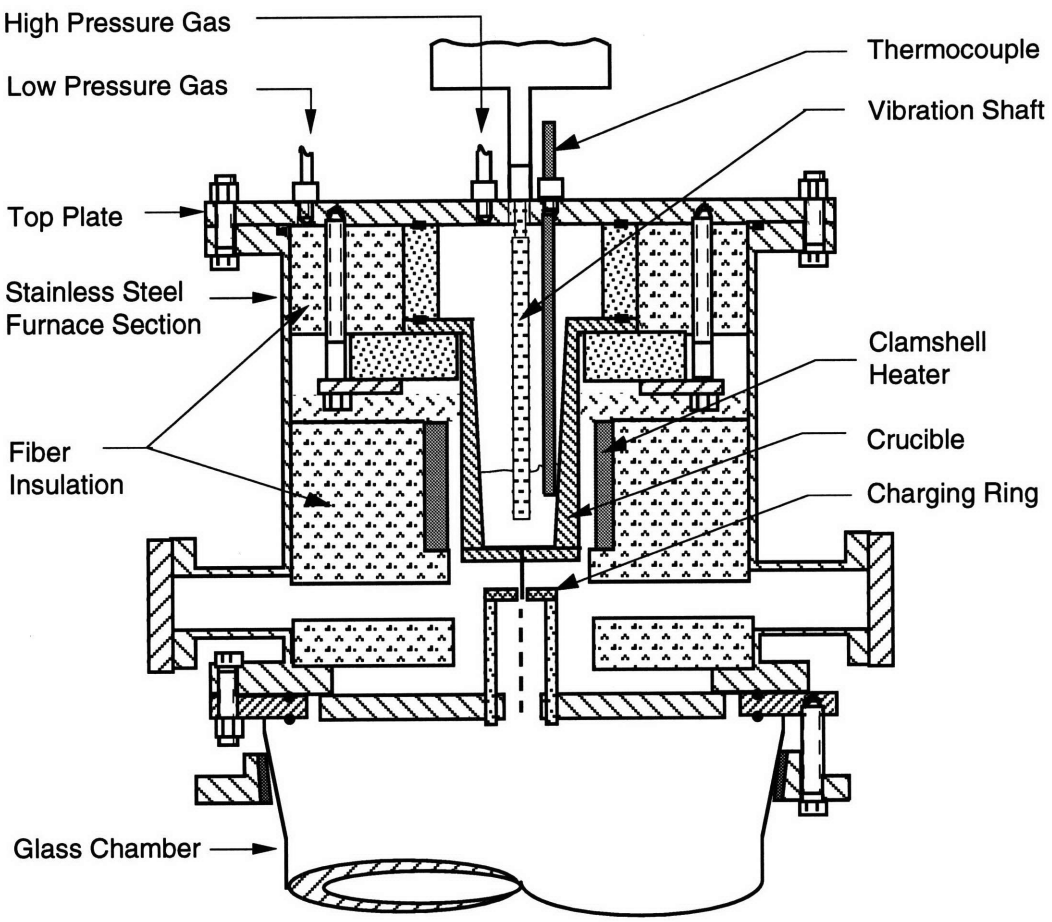

Figure 2.3 Schematic diagram of the high-temperature droplet generator.

formation, $\Delta G^{o}_{Al_2O_3}$, for aluminum oxide is given in calories by [Kubaschewski and Alcock 1979]:

$$\frac{4}{3}\mathrm{Al(l)} + \mathrm{O_2(g)} = \frac{2}{3}\mathrm{Al_2O_3(s)} \tag{2.1}$$

and

$$\Delta \mathrm{G}^{\mathrm{o}}_{\mathrm{Al_2O_3}} = -405{,}760 - 3.75T\log T + 92.22T \tag{2.2}$$

where T is the temperature in K at which the reaction takes place. The equilibrium partial pressure of oxygen, P_{O_2}, above which aluminum oxide is formed is calculated from:

$$P_{O_2} = \exp\left(\frac{\frac{2}{3}\Delta G^{o}_{Al_2O_3}}{\mathrm{R}T}\right) \tag{2.3}$$

Table 2.1 Ceramic foam filters tested in the UDS apparatus.

Manufacturer	Material	Pore Density	Height
Selee Corp.	ps-zircon	45 ppi	13 mm
Selee Corp.	ps-alumina	60 ppi	13 mm
Hi-Tech Ceramics	alumina	80 ppi	10 mm
Vitre-Cell Inc.	silicon carbide	100 ppi	3 mm
Vitre-Cell Inc.	silicon carbide	100 ppi	16 mm

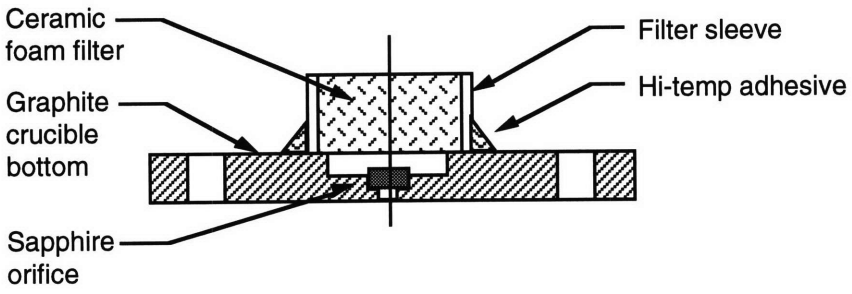

Figure 2.4 Schematic diagram of filter placement on top of crucible bottom and above orifice.

where R is the universal gas constant and equal to 1.987 x 10^{-3} kcal/mol K [Ragone 1995]. Thus, from Equations (2.2) and (2.3), a partial pressure of oxygen less than 2.4 x 10^{-52} atm must be achieved to prevent oxidation of aluminum at 932 K (melting point of Al). In comparison, the P_{O_2} for the formation of stannic oxide (SnO_2) is two orders of magnitude greater at 3.9 x 10^{-50} atm at 505 K (melting point of Sn).

2.2 Filtration of the Aluminum Melt

It was speculated that the stream flow was being disrupted by oxide inclusions that form in the crucible during melting and eventually block the orifice. The charge of material placed in the crucible is made up of several pieces of aluminum or its alloy. Each individual piece is covered by an oxide skin that will remain as inclusions in the melt. To stabilize the aluminum stream, a filter was placed inside the crucible just above the orifice as shown in Figure 2.4. Several different ceramic filters, including aluminum oxide and silicon carbide foam filters, were tested and are listed in Table 2.1.

Aluminum filtration is commonly practiced in casting foundries to improve product quality. The continuous casting of Al-alloys typically utilizes a filter bowl lined with 2" thick, 40 pores per linear inch (ppi), ceramic foam, corresponding to a mean pore size of

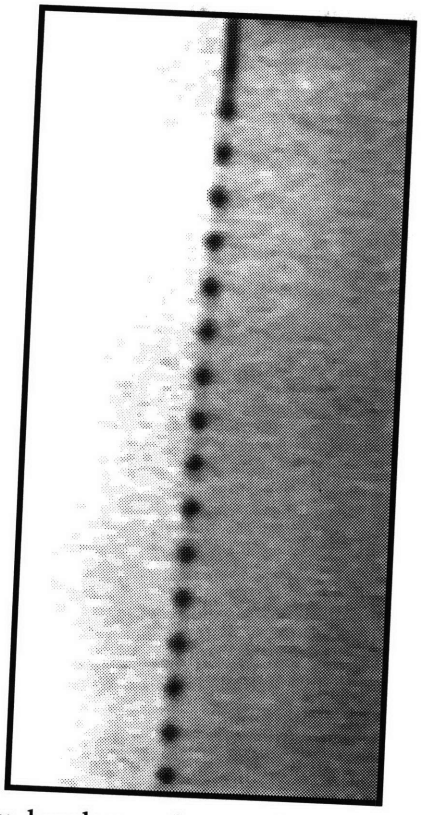

Figure 2.5 Uniform break-up of pure aluminum jet achieved using a 100 μm orifice and 16 mm tall, SiC filter, operating with 138 kPa driving pressure and 21 kHz vibration frequency.

1.5 mm. Filtering through a "deep bed" can effectively capture particles that are nearly four times smaller than the pores [Aubrey and Dore 1993]. A series of experiments were performed to test the effectiveness of the commercially available filters in Table 2.1. Filters with less than 100 ppi (i.e., pore sizes greater than 0.5 mm) did not result in any significant improvement in stream stability. Experiments confirmed that the depth of the filter plays an important role. A 100 ppi filter that was 3 mm tall was ineffective. However, by increasing the height of a 100 ppi, silicon carbide filter to 16 mm, the uniform break-up of a stable stream of aluminum was first achieved. A recorded image of the break-up is shown in Figure 2.5. Nonetheless, the repeatability of the success was limited and orifice clogging problems persisted. Energy dispersive spectrometry (EDS) analysis with a scanning electron microscope (SEM) of a clogged orifice detected silicon carbide particles contaminating the aluminum melt. Although inexpensive, silicon carbide filters have relatively low mechanical strength and are easily damaged in handling or in use. Particles from the filter material may have detached and clogged the orifice.

2.3 Implementation of Gas Purification System

The next option was to spray without the filter and with a larger orifice diameter. The orifice diameter was increased from 100 μm to 150 μm, and to 200 μm. Erratic stream wandering decreased, but intermittent stream thinning continued to be experienced and hence, uniform break-up could not be sustained. It was then concluded that the amount of oxygen in spray chamber was the source of non-ideal processing conditions. The oxygen level in the chamber was typically greater than 30 ppm.

Not only is the material in the crucible oxidizing but also the molten stream of aluminum that exits from the orifice. If oxide patches develop immediately around the aluminum jet as it exits, they could effectively pinch or constrict the jet flow depending on the amount of oxide build-up. This type of erratic flow obstruction can easily explain the jumpy stream behavior and stream thinning observed when spraying aluminum alloys.

Consequently, modifications were made to the system and operating procedure in order to minimize the oxygen and water vapor content in the spray chamber. These changes decreased the oxygen level by nearly two orders of magnitude, from 30 ppm to less than 0.5 ppm. Although at this level oxidation is not completely prevented, the reduced amount of oxide build-up allows for the vibration imposed on the jet to control the break-up of the aluminum jet. Furthermore, as shown earlier, the partial pressure of oxygen to prevent the oxidation of liquid tin is about two orders of magnitude greater than that of liquid aluminum. As a result, the uniform break-up an aluminum jet was finally achieved using 150 and 200 μm diameter orifices. The new gas purification system, which is described below, has consistently produced stable jet behavior and uniform jet break-up.

The current UDS apparatus used to produce uniform droplet sprays of aluminum and its alloys is shown in Figure 2.6. The high-temperature droplet generator designed by Abel was not modified except for the crucible. A stainless steel (AISI 304) crucible body coated with a boron nitride paint was used instead of the graphite crucible body to reduce the chance of metal leaking from the crucible. In addition, since stainless steel has a higher thermal conductivity than graphite, the time required for melting the material, and hence time for oxidation, is decreased.

The gas purification system was installed. It consists of copper tubing which replaced the previous plastic hoses, a molecular sieve with type 13x pellets (Alpha Aesar #33550) to dessicate the oil and water vapor, a sponge titanium furnace (Centorr/Vacuum Industries #2B-20-Q) heated to 800°C to remove oxygen and water vapor, an oxygen analyzer (Illinois Instruments #2550), and a diaphragm pump (Neptune Products #4K) that circulates the chamber gas through the purifying components. The key to successful

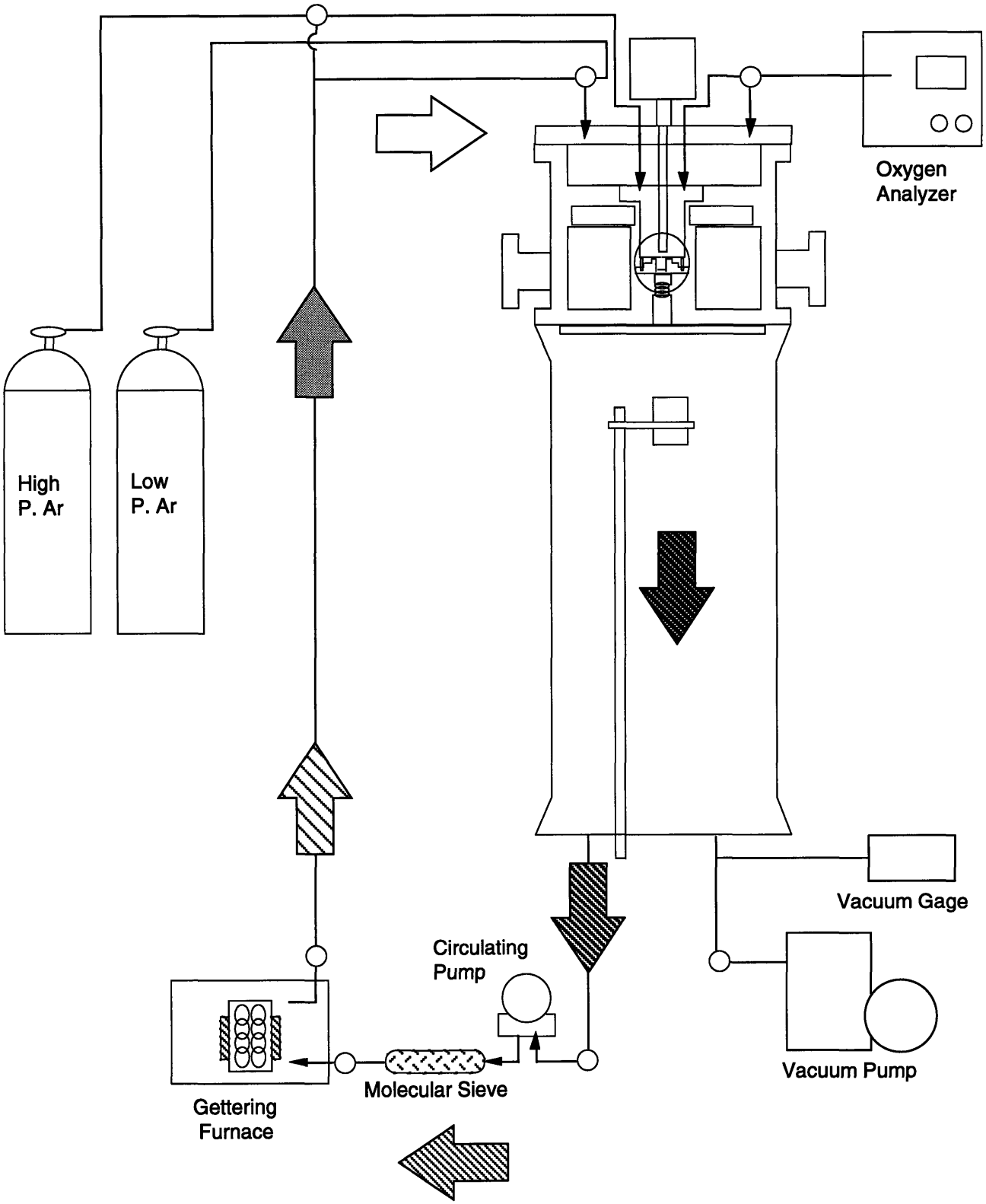

Figure 2.6 High temperature UDS apparatus with gas purification system.

purification lies in the titanium furnace, commonly referred to as an oxygen getter. The principle behind the oxygen getter is to provide a source of material, such as titanium or zirconium, that has greater affinity to oxygen than the molten aluminum that is being sprayed into the chamber. The hot titanium reacts with the oxygen and water vapor in chamber to provide a non-oxidizing environment for the liquid aluminum.

2.4 Spray Procedure

The working procedure was developed and strictly followed. The sensitivity of each step to achieving uniform jet break-up was not determined. However, every step was treated as a precaution to minimize the oxidation of aluminum.

2.4.1 Material preparation

Pure aluminum and three different alloys: Al-4.5wt% Cu, Al-4.3wt% Fe, and Al-10wt% Si, were tested with the UDS apparatus and gas purification system. The alloys were supplied by the Aluminum Company of America (ALCOA) and the Oak Ridge National Laboratory. The cleanliness of the cast alloys is very important to ensure a stable stream throughout the entire experiment. The Al-Fe and Al-Si alloys which were cast by ALCOA by induction melting with an argon/chlorine flux produced a significantly more stable stream and break-up than did the Al-Cu alloy which was melted in an induction furnace in air. The following procedure is the same for each aluminum alloy.

The oxide layer of the cast material was removed, either by turning down cast cylindrical rods on a lathe or grinding the oxide layer away with a belt sander or dremmel tool. The material was then cut into pieces sized about 5 cm x 1 cm x 1 cm to fit inside the crucible. The pieces were deburred and then cleaned with methanol.

2.4.2 Set-up of the droplet generator

For each run, the two-part crucible is disassembled and cleaned thoroughly with a vacuum cleaner to remove any material debris. The boron nitride coating (ZYP Coatings) inside the stainless steel crucible is checked for complete coverage. A new sapphire orifice is cemented into the orifice pocket on the crucible bottom with high temperature ceramic adhesive (Cotronics #904Zr). The cement is cured for 4 hours in an oven at 100°C. The graphite crucible bottom and graphite gasket are also coated with boron nitride. About 100 grams of cleaned aluminum charge are placed in the crucible and sealed tightly with stainless steel screws. Because the crucible and charging ring are part of separate apparatus sections, the charging ring must be centered with respect to the orifice at the bottom of the crucible each time. After the charging ring is centered, the furnace section is fastened to the

top of the glass chamber. Then, the crucible top plate is fastened on top of the furnace section.

2.4.3 Gas purification procedure

The gas purification system and the assembled droplet generator unit are connected by copper tubing. The chamber, tubing, and droplet generator are evacuated with a roughing pump to about 500 millitorr. Then, the droplet generator is baked out to remove water vapor by heating the crucible to 250°C while maintaining vacuum. At 250°C, the heater is turned off and the vacuum pump continues to evacuate the system. When the vacuum pressure in the chamber is about 150 millitorr, the system is back-filled with argon gas to the gauge pressure of 35 kPa (5 psig). This process is repeated two more times. After the third purging, the system is filled to 35 kPa (5 psig) and the level of oxygen in the system is measured with the oxygen analyzer. If there is less than 50 ppm of oxygen, the recirculating pump and oxygen getter are turned on to further purify the chamber gas. If not, then the system is evacuated and back-filled again. More than 50 ppm of oxygen can fully saturate the hot titanium charge and render it useless. The recirculating pump draws gas from the chamber and crucible, and forces the gas through the molecular sieve and oxygen getter with a flow rate around 6 liters per minute and maximum pressure of 70 kPa. The gas is purified and fed back into the system, and periodically measured with the oxygen analyzer.

Gettering continues for about 1 hour, or until the oxygen level reaches a steady state, typically below 0.5 ppm. At this point, the crucible heater is turned on to melt the aluminum material to 750°C. Then, the bypass valve which connected the crucible and chamber during purification is turned off. The getter continues to purify the chamber gas throughout the experiment.

2.5 Powder Size Distribution

In order to verify that the UDS process can produce uniform droplets of aluminum, the molten droplets were allowed to completely solidify in flight. At the bottom of the 1-meter tall spray chamber, powders were collected and then measured with an optical microscope. The uniformity of droplet size is important since it allows the process to be modeled without any statistical analysis. From a random sample group of 53 Al-4.5wt% Cu powders produced by the UDS process in a single run, the standard deviation was measured to be ± 4.5 μm. The powders are shown in Figure 2.7(a) and the size distribution in Figure 2.7(b). This deviation is not significant enough to invalidate the solidification models based on uniform droplet size as discussed in the following chapter.

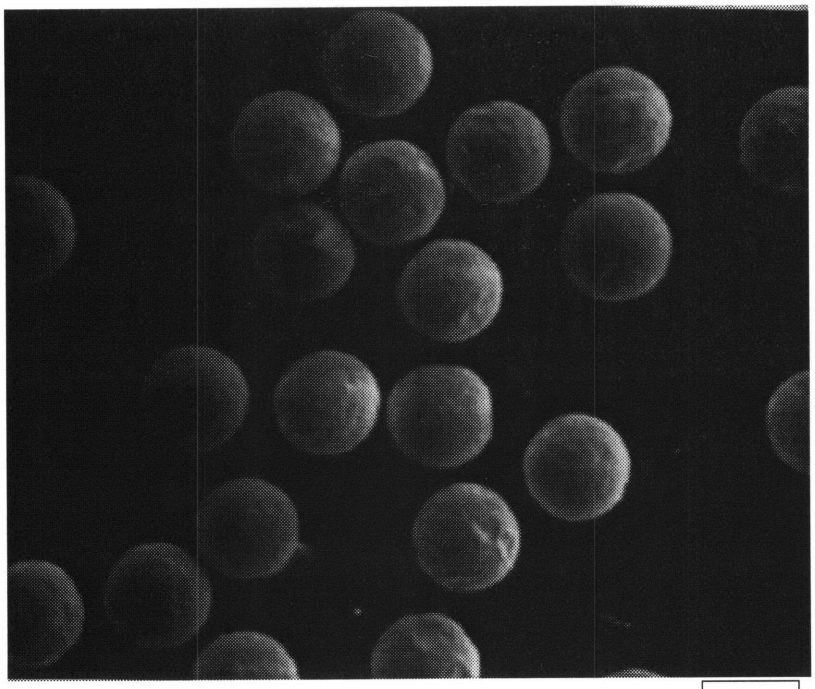

(a)

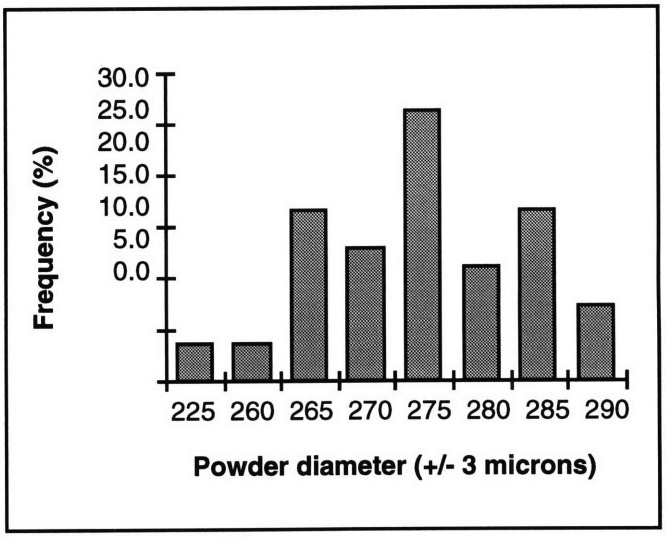

(b)

Figure 2.7 (a) SEM pictures of Al-4.5wt% Cu powders produced by the UDS process, and (b) their size distribution. Sample mean is 274.7 µm in diameter with a standard deviation of 4.5 µm.

Chapter 3 DROPLET SOLIDIFICATION MODEL

Before the aluminum droplet spray can be applied to the production of parts with homogeneous, non-porous, fine equiaxed microstructure, the thermal history of the droplets must be understood. The incoming thermal state of the droplets at impact with the substrate significantly affects the degree of droplet consolidation as well as the microstructural grain size, which in turn determine the final material property of the sprayed part. The thermal state of a solidifying droplet is defined by its temperature and volume fraction of solid.

A Newtonian heat transfer model has been employed to predict the enthalpy loss of the droplet due to convection during flight. The change in enthalpy is related to the droplet temperature. Given the droplet temperature, the increase in solid fraction of the droplet is assumed to be governed by the Scheil equation for equilibrium solidification. Knowledge of the droplet velocity and position is a prerequisite for determining the heat transfer coefficient. Therefore, the droplet trajectory is computed simultaneously with the heat transfer and solidification models.

3.1 Jet Break-Up

In the UDS process, droplet size is predicted by the theory of instability for a laminar liquid jet. A liquid jet will break up into a train of droplets due to capillary instability from natural disturbances. However, when a perturbation is imposed on the jet at a specific frequency, the jet will break up into uniform droplets. Lord Rayleigh [1878] developed a relationship between the perturbation wavelength, λ, and the growth rate of perturbation for inviscid flows. The maximum growth rate occurs when the dimensionless wavelength, λ/d_j, is:

$$\frac{\lambda}{d_j} = 4.508 \tag{3.1}$$

where d_j is the jet diameter and the λ is the jet velocity divided by the frequency of perturbation. For example, a liquid jet of aluminum, 150 μm in diameter, with a jet velocity of 5 m/s, will break up into uniform droplets at a vibration frequency near 7.4 kHz. Passow [1992] and Yim [1996] have shown that the uniform break-up frequencies in the UDS process closely follow Equation (3.1) for jet diameters ranging from 50 μm to 400 μm. Using the dimensionless wavelength, the droplet size can be determined through a simple mass conservation principle. For a given density, the volume of a liquid cylinder

whose height is equal to the perturbation wavelength and whose diameter is the jet diameter, must equal the volume of the spherical droplet formed. The droplet diameter, d_d, is predicted by the following expression:

$$d_d = d_j\left(\frac{3\lambda}{2d_j}\right)^{1/3} \tag{3.2}$$

Therefore, by substituting Equation (3.1) into Equation (3.2), the droplet diameter is found to be approximately two times the jet diameter.

3.2 Droplet Trajectory Model

The dynamic behavior of the traveling droplets is determined by balancing all the forces acting on the droplet. In addition to gravity and drag forces, the droplet is also subject to a Coulomb repulsion force as shown in Figure 3.1. To prevent droplet coalescence during flight, the stream of droplets are inductively charged through a charging plate. After charging, the droplets remain aligned in a stream until inherent disturbances and electrical repulsion cause them to deviate from the centerline and scatter. The total Coulomb force on a droplet is derived by summing all the Coulomb forces imposed by its neighboring droplets:

$$\vec{F}_c = \frac{1}{4\pi\varepsilon_o}\sum_{j=0}^{N}\frac{q_d^2}{\vec{r}_j} \tag{3.3}$$

where ε_O is the permittivity of free space, N is the total number of droplets in flight, q_d is the electrical charge carried by each droplet, and r_j is the distance between the droplet and droplet j. The droplet scattering also affects the drag force since the drag experienced by a droplet traveling with neighboring droplets is different than that of an isolated droplet in flight [Mulholland et al 1988]. In general, the drag force is defined by:

$$\vec{F}_d = \frac{1}{8}C_D\pi\rho_m d_d^2|\vec{v}_d|\vec{v}_d \tag{3.4}$$

where C_D is the drag coefficient, ρ_m is the density of the metal, and v_d is the droplet velocity. The drag coefficient depends on the distribution of the droplets. Let l_d be the spacing between droplets of diameter d_d . When l_d/d_d approaches infinity, the drag

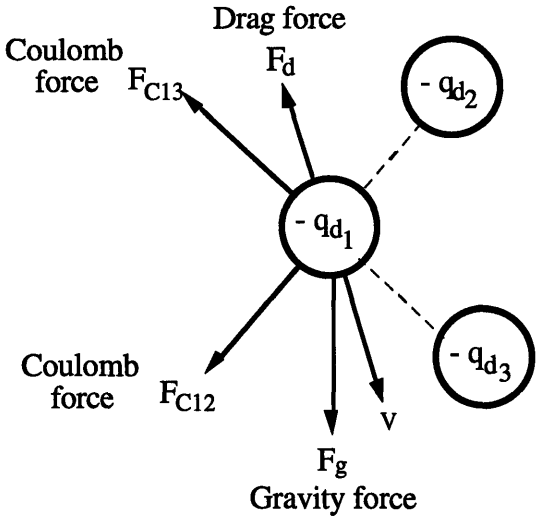

Figure 3.1 Forces acting on a single droplet.

coefficient of an isolated liquid sphere in flight, C_{D_S}, is given by:

$$C_{D_s} = 0.28 + \frac{6}{\sqrt{\mathrm{Re}}} + \frac{21}{\mathrm{Re}} \tag{3.5}$$

where Re is the Reynolds number. The drag coefficient for a droplet in an aligned stream of uniformly size droplets, C_{D_A}, was determined by Mulholland et al [1988] to be:

$$C_{D_A} = \left[\left(C_{D_{1+}} \right)^{-n} + \left(C_{D_s} \right)^{-n} \right]^{-1/n} \tag{3.6}$$

where $C_{D_{1+}}$ is the drag coefficient as the ratio of droplet spacing to droplet diameter approaches one (l_d/d_d->1) and n is an empirical parameter that equals 0.678 ± 0.07. $C_{D_{1+}}$ is expressed by:

$$C_{D_{1+}} = C_{D_1} + \frac{a}{\mathrm{Re}}(l_d/d_d - 1) \tag{3.7}$$

where a is another empirical parameter that is equal to 43.0 ± 15.4 and C_{D_1} is the drag coefficient when l_d/d_d equals to 1. C_{D_1} depends on the drag coefficient for a rod, $C_{D_{rod}}$,

and the drag coefficient for an isolated sphere as given by:

$$C_{D_1} = \left[\left(C_{D_{rod}} \right)^{-n} - \left(C_{D_s} \right)^{-n} \right]^{-1/n} \tag{3.8}$$

where $C_{D_{rod}} = 0.755/Re$.

Therefore, when the droplet spacing is initially less than one droplet diameter, the drag coefficient is chosen to be a combination of C_{D_s} and C_{D_A}:

$$C_{D_r} = (1 - r/r_d) C_{D_A} + (r/r_d) C_{D_S} . \tag{3.9}$$

When the droplets have scattered sufficiently such that they are more than one droplet diameter apart, the drag coefficient for an isolated sphere in Equation (3.6) is used to determine the drag force. Finally, the equation of motion for a droplet can be written as:

$$m_d \frac{d\vec{v}_d}{dt} = \vec{F}_g + \vec{F}_d + \vec{F}_c \tag{3.10}$$

where $\vec{F}_g$ is the gravity force. The gravity force is merely the product of the droplet mass, m_d, and the gravity constant, g:

$$\vec{F}_g = -m_d g \vec{z} \tag{3.11}$$

where $\vec{z}$ is the unit vector in the vertical direction.

The velocity and position of the droplet are solved explicitly using a fourth-order Runga-Kutta numerical integration. The initial droplet velocity is assumed to be the initial jet velocity, $v_{j,i}$, which can be determined by Bernoulli's equation:

$$v_{j,i} = K_d \left(\frac{\Delta p}{2\rho_m} \right)^{1/2} \tag{3.12}$$

where Δp is the pressure differential between the crucible and the chamber, and K_d is the exit coefficient from an orifice. The exit coefficient is determined experimentally for a specific orifice size and shape and melt material by measuring the mass flowrate. For aluminum alloys, the exit coefficient measured for the 155 μm orifice is 0.82.

The droplet trajectory model was developed for the UDS process by Passow [1992] and Abel [1994]. To validate the model, the velocities of 200 μm tin droplets were

measured using high speed photography by Kim [1996]. The measurements showed good agreement with droplet velocity as a function of driving pressure, charging voltage, orifice diameter, and flight distance.

3.3 Droplet Thermal Model

3.3.1 Droplet heat transfer

The rate of change in enthalpy of a droplet during flight is determined by the amount of heat lost to the surrounding gas through convection and radiation. The enthalpy loss of the droplet can be given by:

$$m_d \frac{dH}{dt} = h A_d^s (T_d - T_g) + \sigma \varepsilon A_d^s (T_d^4 - T_g^4) \tag{3.13}$$

where H is droplet enthalpy per unit mass, h is the convective heat transfer coefficient, A_d^s is the droplet surface area, σ is the Stefan-Boltzman constant, ε is emissivity, T_d is the droplet temperature, and T_g is the gas temperature. The Biot number for 300 μm aluminum droplets is estimated to be on the order of 2×10^{-4}, which is much less than the 0.1 criterion for Newtonian cooling [Rolland 1996]. Therefore, the heat conduction inside the droplet can be ignored and the droplet temperature can be treated as spatially uniform. Compared to the heat convection term, the heat loss due to radiation for aluminum alloys is at least two orders of magnitude less and can also be neglected. The gas temperature in the chamber was measured and expressed as a function of flight distance.

The convective heat transfer coefficient for a traveling sphere is given by the Ranz-Marshall correlation:

$$h = \frac{k_g}{d_d}(2.0 + 0.6 \mathrm{Re}^{1/2} \mathrm{Pr}^{1/3}) \left(\frac{C_{g(avg)}}{C_g} \right)^{0.26} \tag{3.14}$$

where k_g is the gas thermal conductivity, $\mathrm{Re}=\rho_g v_d d_d / \mu_g$ is the Reynolds number of flow over a sphere, $\mathrm{Pr}=\mu_g C_g / k_g$ is the Prandtl number, C_g is the gas heat capacity at the gas temperature, and $C_{g(avg)}$ is the gas heat capacity at the average temperature of the gas and droplet. When the droplet is traveling in an aligned stream, the heat transfer coefficient is adjusted by the ratio of C_{D_r} / C_{D_s}, where C_{D_r} and C_{D_S} are given by Equations (3.9) and (3.5) respectively [Passow 1992]. Therefore, the adjusted heat transfer coefficient is

expressed by:

$$h_{aligned} = \frac{C_{D_r}}{C_{D_s}} h \tag{3.15}$$

From Equations (3.13), (3.14), and (3.15), the rate of enthalpy loss in the droplet can be computed at a given droplet temperature. In general, the enthalpy per unit mass of a binary alloy is determined by the Lever rule to be:

$$H = (1 - f_s)H_l + f_s H_s \tag{3.16}$$

where f_s is the solid fraction, H_l is the enthalpy of the liquid portion, and H_s is the enthalpy of the solid portion. H_l and H_s assume the heat of mixing effect to be negligible and are given by:

$$H_l = (1 - \overline{C}_l)H_{l,1}(T) + \overline{C}_l H_{l,2}(T) \tag{3.17}$$

$$H_s = (1 - \overline{C}_s)H_{s,1}(T) + \overline{C}_s H_{s,2}(T) \tag{3.18}$$

where $\overline{C}_l$ and $\overline{C}_s$ are the average weight compositions of the solute in the liquid and solid portions, $H_{l,1}$ and $H_{l,2}$ are the enthalpies of the solvent and solute in the liquid phase, and $H_{s,1}$ and $H_{s,2}$ are the enthalpies of the solvent and the solute in the solid phase, respectively.

When the droplet is fully liquid, its enthalpy is directly related to the droplet temperature since $\overline{C}_l$ is fixed at the original composition, C_o, of the alloy. Equation (3.16) reduces to:

$$H = H_l = (1 - C_o)H_{l,1}(T) + C_o H_{l,2}(T) \quad \text{for } T > T_l \tag{3.19}$$

However, when the droplet temperature drops below the liquidus temperature, T_l of the alloy, the droplet contains both solid and liquid phases. The enthalpy of a mushy droplet then becomes function of the solid fraction, solid composition, liquid composition, and temperature. Therefore, a model is needed to describe the solute redistribution that takes place during solidification; the Scheil equation is chosen.

3.3.2 Droplet solidification

From a survey of rapid solidification literature, aluminum alloy droplets larger than 200 μm in diameter typically avoid undercooling [Rolland 1996, Grant and Cantor 1995, Lee and Ahn 1994]. Therefore, nucleation in the droplet is assumed to begin at the liquidus temperature. After nucleation, the redistribution of the solute during solidification progresses according to the Scheil equation which assumes complete diffusion in the liquid, no diffusion in the solid, and local equilibrium at the solid-liquid interface. Quantitatively, these assumptions signify that the amount of solute rejected when an incremental amount of solid is formed is equal to the resulting increase of solute in the liquid. This balance is:

$$(C_l - C_s^*)df_l = f_l dC_l \tag{3.20}$$

where C_s^* is the weight composition of the solute at the solid interface. Equilibrium at the solid-liquid interface requires that C_l and C_s^* be determined by the phase diagram of the binary alloy. Thus, the solid fraction can be expressed as a function of temperature alone. Consequently, Equation (3.18) can be solved implicitly now.

Although all the assumptions of the Scheil equation are generally not applicable to rapid solidification, the equation is frequently adopted to predict the estimated solid fraction because of its simplicity [Grant and Cantor 1995, Lee and Ahn 1994, Lavernia et al 1992].

3.4 Simulation of Droplet Solidification

The droplet solidification model was numerically simulated together with the droplet trajectory model using MATLAB. The program was originally designed for hypoeutectic Zn-Sn alloys by Chen [1996]. The program has since been modified for the hypoeutectic Al-4.5wt% Cu alloy and hypereutectic Al-4.3wt% Fe alloy, and can be found in Appendix A. The physical properties and phase diagram of the Al-Cu and Al-Fe alloy systems used in the simulation can be found in Appendix B. The simulation results are shown for the different alloys in Figures 3.2 and 3.3.

The droplet thermal history shows how the droplet undergoes three different cooling regimes. Initially, the droplet is superheated and heat is extracted through convection in an aligned stream of droplets. Then, the rate of convective heat loss increases in the second regime after the droplets start to scatter such that the spacing between droplets is greater than one. Solidification begins at the liquidus temperature of the alloy. During solidification, the cooling rate decreases as latent heat is released from the

newly formed solids. The droplet continues to solidify until the liquid is completely depleted. The cooling rate can be calculated from Figures 3.2 and 3.3 by the product of the rate of change in temperature with respect to flight distance and the droplet velocity:

$$\frac{dT}{dt} = \frac{dT}{dz}\left(\frac{dz}{dt}\right) \tag{3.21}$$

3.5 Cooling Rates Determined by Dendrite Arm Spacing

Refinement of grain size has been shown to result from increasing cooling rates during solidification [Lavernia et al 1992]. Previous research has established an empirical correlation between secondary dendrite arm spacing (*DAS*) and cooling rate (*dT/dt*) as

$$DAS = B\left(\frac{dT}{dt}\right)^{-n} \tag{3.22}$$

In general for aluminum alloys, n is about 1/3 and B is 50 $\mu m(Ks^{-1})^n$ over the range 10^5 to 10^6 Ks^{-1} [Stone and Tsakirpoulos 1992]. This power law relationship is often used to confirm that cooling models accurately predict the droplet temperature within an order of magnitude. Secondary DAS can be substituted with cell size for cellular solidification morphologies. The DAS has been reported to be nearly independent of fraction solid [Grant and Cantor 1995]. Therefore, the cooling rate during liquid phase cooling can be approximated by the dendrite arm spacing.

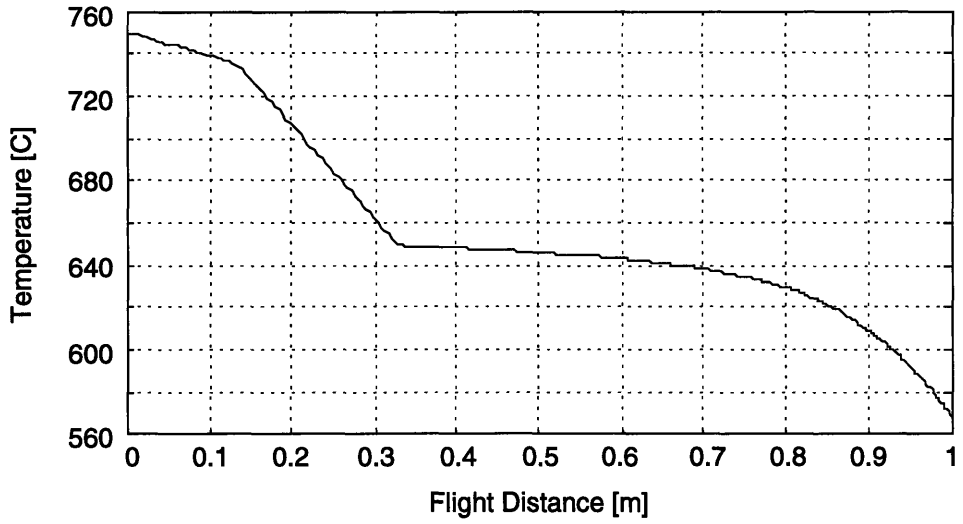

(a)

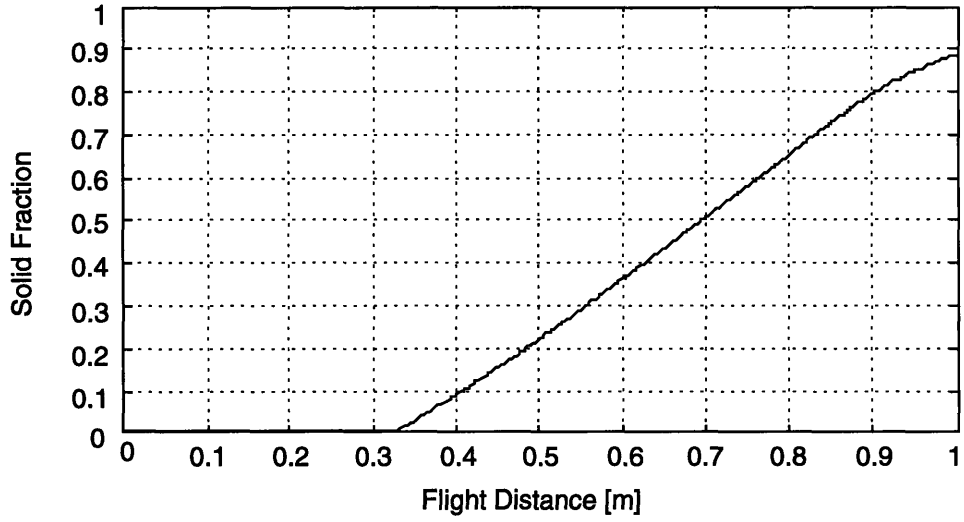

(b)

Figure 3.2 Simulation results for Al-4.5wt% Cu with 275 μm diameter droplet, (a) droplet temperature vs. flight distance, (b) droplet solid fraction vs. flight distance.

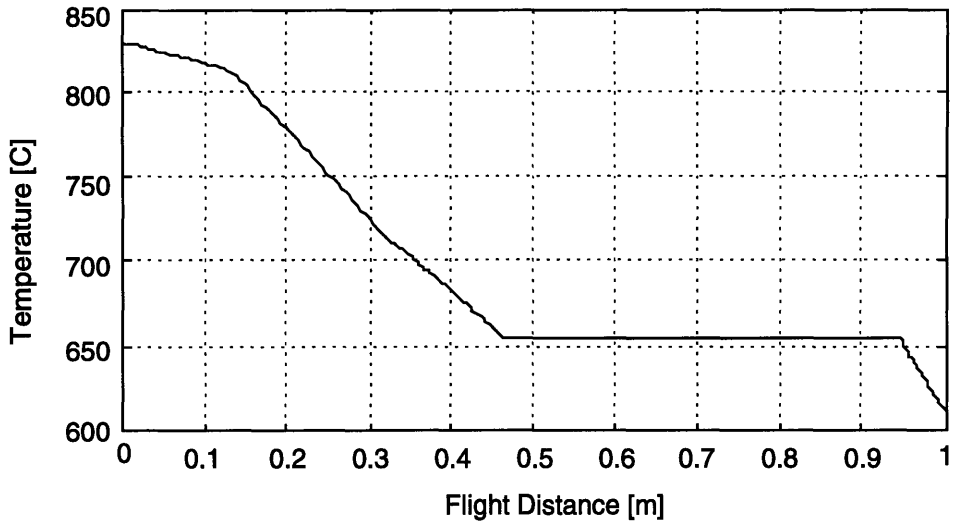

(a)

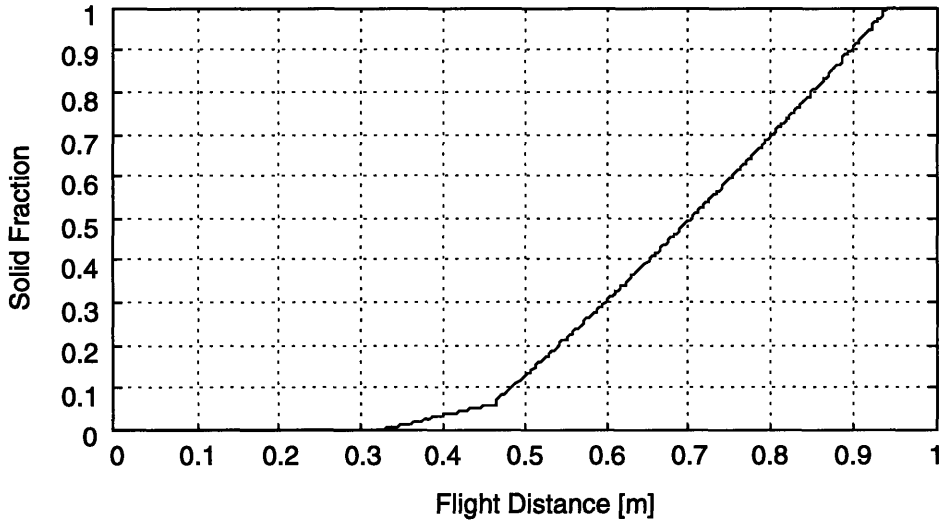

(b)

Figure 3.3 Simulation results for Al-4.3wt% Fe with 250 μm diameter droplet, (a) droplet temperature vs. flight distance, (b) droplet solid fraction vs. flight distance.

Chapter 4 DROPLET SOLID FRACTION MEASUREMENT

The thermal state of a droplet is defined by its temperature and liquid fraction. A solidification model to predict the droplet thermal state in the UDS process was presented in the previous chapter. This chapter describes the experimental study performed to validate the model for aluminum alloys. Measuring either droplet temperature or liquid fraction directly during flight is very difficult. In one study, a pair of color pyrometers were used to measure the cooling curve of a levitated molten Fe-25wt% Ni droplet [McDevitt & Abbaschian 1986]. However, the high reflectivity of aluminum and the high sensitivity of surface emissivity to oxidation, would cause infrared temperature measurements to be ambiguous [Rolland 1996]. Some investigators have instead measured enthalpy flux with calorimetric devices in gas-atomized sprays [Bewlay and Cantor 1990]. However, non-adiabatic calorimeters often require a fine degree of calibration to account for enthalpy losses to the environment [Sahu 1994].

To validate the solidification model of the UDS process described in Chapter 3, Chen [1996] developed an experimental methodology to measure the solid fraction of droplets at various flight distances. Molten droplets of Zn-20wt% Sn alloy were rapidly quenched in flight and the microstructure of the quenched droplets were examined metallographically. Due to the large difference in cooling rates, it was possible to distinguish the solid dendritic phase formed during flight from the solids formed upon quenching. The quenching action halts the microstructural evolution in the droplet to preserve the droplet solid fraction at a specific flight distance. Using 288 μm droplets, a good agreement between his simulation and experimental results confirmed that the droplet thermal state can be accurately predicted in the UDS process for tin alloys. However, the droplet solidification behavior is strongly dependent on the composition of the alloy. This work is an extension of Chen's research to verify that the solidification model based on Scheil's equation can be applied to predict the thermal state of aluminum alloy droplets.

4.1 Material Selection

Two different aluminum alloys were chosen for the solid fraction study: Al-4.5wt% Cu and Al-4.3wt% Fe. Al-Cu is the base alloy of the 2xxx series of commercial aluminum alloys used for automotive parts and aircraft structure. Thus, Al-4.5wt% Cu alloy is commonly used in gas-atomized spray modeling because of its well-documented material properties and undercooling behavior [Grant and Cantor 1995, Lu et al 1994]. Furthermore, the

literature has established a strong correlation between cooling rate and secondary dendrite arm spacing for Al-4.5wt% Cu [Stone and Tsakiropoulos 1992]. .

Al-4.3wt% Fe was chosen for its low solid solubility to help distinguish solids formed prior to quenching. The solid solubility of Fe in Al is less than 0.05%; Al will reject Fe into the liquid phase as it solidifies. The undercooled regions of Al-Fe formed during recalescence are also easily identified by featureless zones [Cotton and Kaufman 1991]. Commercially, iron is added to aluminum to improve high temperature properties for aerospace applications.

4.2 Experimental Apparatus and Procedure

A uniform droplet spray of aluminum alloy is created with the high-temperature droplet generator in a purified gas environment, as described earlier in Chapter 2. Inside the spray chamber, a droplet collecting unit is placed as shown in Figure 4.1. Five collectors are attached to a stainless steel shaft at different levels of flight distance measured from the bottom of the crucible. The collectors are spaced 40 mm vertically and about 30 degrees rotationally apart from each other. The base of each collector is an aluminum piece (25 mm x 20 mm x 3 mm) on which a cold substrate, such as a smooth carbon steel razor blade or a 5 ml stainless steel cup filled with diffusion pump oil, is mounted. The top collector is located at 300 mm below the orifice. After uniform break-up is obtained with the droplet spray, the shaft is quickly rotated a full revolution to collect droplets at different flight distances.

The spray chamber also contains two 125 ml stainless steel beakers. One of the stainless steel beakers is initially placed directly in-line with the droplet stream to collect the spray while the vibration frequency and amplitude are adjusted to produce uniform jet break-up. After the processing conditions are tuned, the second beaker is used to measure the mass flow rate by collecting the spray for 30 seconds. The accumulated mass in the beaker is weighed and the initial jet velocity for the experiment can be obtained. Another beaker is also placed at the bottom of the chamber to collect powders from which the representative powder size distribution is gathered.

4.3 Sample Preparation

The droplet collecting unit is removed from the spray chamber after the droplet generator cools and is removed. If oil is used as the quench medium, each stainless steel cup that contains the quenched droplets is emptied onto a microscope slide. The oil is wicked off the slide with absorbent paper. The powders are doused in acetone a few times to remove

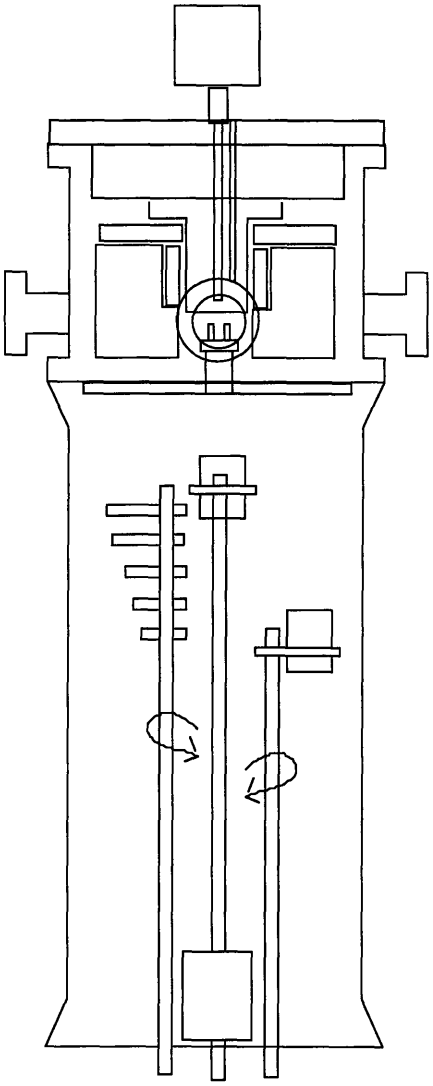

Figure 4.1 Experimental set-up for droplet solid fraction experiments.

the remaining oil. Five randomly selected powders are transferred from each slide to a thin Teflon mounting base with the aid of an optical microscope. When smooth steel substrates are used, the splats are directly moved from the substrate to the Teflon base. The Teflon base is prepared by applying a very thin layer of epoxi-patch on its top surface to hold the powders or the splats to it. The splats or powders are aligned on the edge of the Teflon base as shown in Figure 4.2 (a). After 24 hours, the epoxy cures and the samples on the Teflon base are examined under an optical microscope with 30x magnification to measure each sample diameter using cross-hairs mounted on x-y tables.

The next step is to cast the samples on the Teflon base in epoxy mold cups for microstructural analysis. The Teflon bases are held upright with plastic mounting clips as

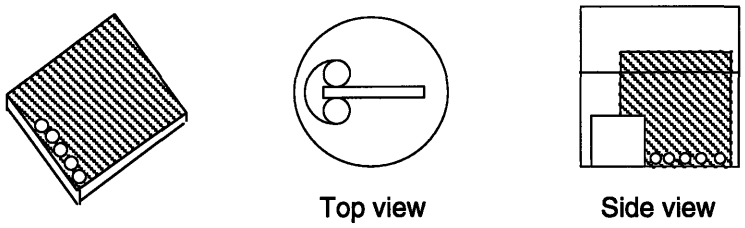

Figure 4.2 Sample preparation for SEM analysis (not to scale).

shown in Figure 4.2 (b). After being cast in epoxy, the splats or powders are successively ground to their center cross-sections using 320, 600, and 800 grit abrasive papers. The center of the splat or powder can be found by grinding the sample until the width of the cross-section is approximately equal to the diameter of the splat or powder Fine polishing is obtained with 6 μm diamond paste and Metadi fluid and then 0.06 μm Mastermet suspension. The samples are chemically etched with Keller's reagent (H_20: 190 mL, HNO_3: 5 mL, HCl: 3 mL, HF(48%): 2 mL) for 10 seconds for the Al-Cu samples and 7 seconds for the Al-Fe samples. After the samples are rinsed and air dried, carbon sputter coating is applied for backscattered electron imaging in a JEOL SEM.

4.4 Image Analysis of Microstructure

By examining the microstructure of the quenched droplets, the solid phase formed prior to quenching is distinguished from the solid phase formed upon impact. The micrographs of the samples are scanned into a computer for image processing to determine the apparent solid fraction. Using image analysis software, the area of the solid portion is outlined and highlighted. The software quantifies the highlighted area of solid as well as the total area of the powder cross-section. The ratio of the values is taken as the solid fraction of the droplet. The average of the solid fractions obtained from the droplets collected at the same flight distance is computed.

4.5 Results

The experimental conditions used to measure the solid fraction of the Al-Cu and Al-Fe droplets are given in Table 4.1. By examining the change in microstructure from a fully liquid droplet to a fully solid powder, a trend can be observed and is correlated to the solid fraction of the droplet. The solid powder cross-sections are also compared with typical microstructures seen in gas atomized powders to determine the degree of microstructural refinement.

Table 4.1 Experimental conditions used to measure droplet solid fraction.

Alloy material	Al-4.5wt% Cu	Al-4.5wt% Cu	Al-4.3wt% Fe
Quench medium	metal substrate	oil	metal substrate
Droplet diameter	295 μm	275 μm	250 μm
Melt temperature	750°C	750°C	830°C
Pressure differential	8 psi	11 psi	8 psi
Vibration frequency	7.3 kHz	7.3 kHz	8.6 kHz
Charging voltage	500 V	600 V	600 V
Oxygen level	0.3 ppm	1.2 ppm	0.4 ppm

4.5.1 Al-4.5wt% Cu powders

Figure 4.3 displays micrographs of the surface and cross-section of a typical 295 μm, Al-Cu powder collected at the bottom of the UDS spray chamber. The droplet surface is overall bumpy with a noticeable pit or two. These pits which are frequently observed in UDS-produced aluminum powders may be due to droplet collision during the later stages in flight or during collection. The general unevenness of the droplet surface suggests that liquid exists at the droplet surface until near the end of solidification. As solidification shrinkage takes place, this liquid is drawn inward, leaving the surface rough [Flemings 1974].

The cross-section microstructure in Figure 4.3 (b) can be characterized by fully developed dendritic solidification which is fairly common in gas-atomized Al-4.5wt% Cu powders of the same diameter. The microstructure is fairly uniform throughout the droplet cross-section. Average secondary dendrite arm spacing is estimated to be 6.3 μm. If microstructure of the powder collected at 1 m is said to be representative of the solid phase formed by in-flight cooling, then it is expected that the droplet microstructure show increasingly dendritic microstructure as it solidifies. This hypothesis is confirmed by the droplets collected at intermediate flight distances.

4.5.2 Substrate-quenched Al-4.5wt% Cu droplets

The microstructures of Al-Cu droplets, with an average diameter of 295 μm, quenched on steel substrates at flight distances of 0.4 m, 0.42 m, 0.46 m, and 0.48 m are shown in Figures 4.4 (a) through (d), respectively. The micrographs are representative of the other cross-sections observed at the same flight distance. The microstructure in Figure 4.4 (a) appears nearly featureless. However, greater magnification reveals a crystalline structure which is either very fine dendrites or cells that are oriented parallel to the direction of heat

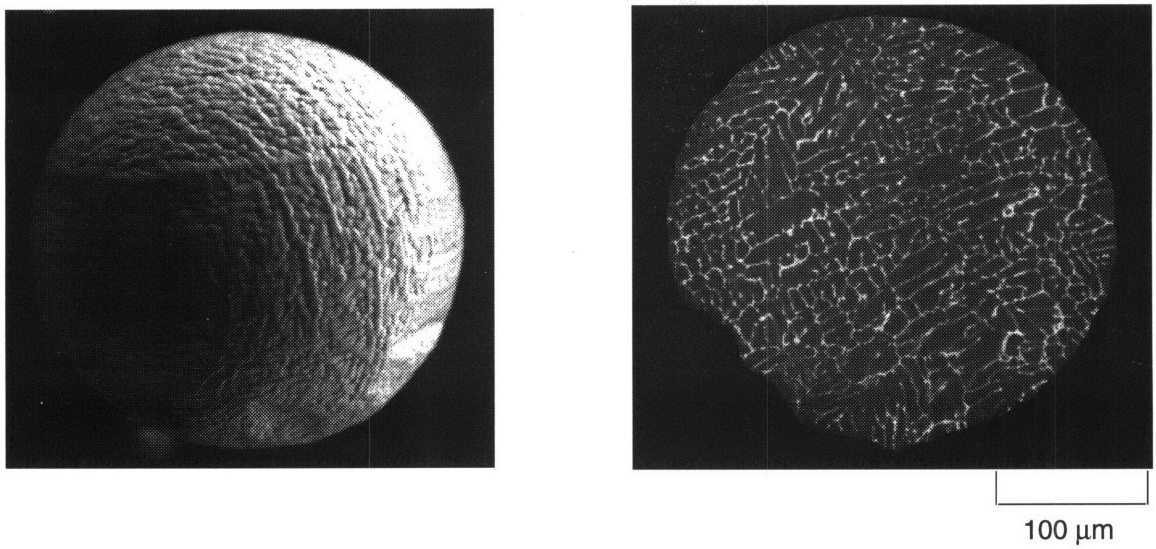

Figure 4.3 Micrographs of the (a) surface and (b) cross-section of 295 μm, Al-4.5wt% Cu powders collected at the bottom of the chamber.

flow. The columnar orientation indicates that solidification occurred after the droplet impacted the substrate since its growth is controlled by the heat flow to the substrate. During the rapid quenching, the solute is not able to segregate from the liquid, which explains why the fine crystalline features are uniformly distributed. Droplets collected at 0.3 m through 0.4 m all show similar microstructure. Therefore, it is concluded that the droplets remain fully liquid above 0.4 m.

At 0.42 m, the first sign of solidification is observed in Figure 4.4 (b). Surrounded by the fine crystalline structure, there exists a coarser dendritic region that reaches from the bottom of the splat to the top surface. Figure 4.4 (c) shows a quenched droplet 0.04 m later in which the dendritic portion has increased and the fine crystalline region has decreased. By 0.48 m, the coarser dendritic structure nearly occupies the entire cross-section as shown in Figure 4.4 (d). Therefore, the observed trend suggests that the fine crystalline region represents the liquid part of the droplet before impact and that the coarser dendritic region is the solid part formed during flight. This assumption is based on the inverse relationship between cooling rate and dendrite arm spacing. Since the liquid of the droplet cools much faster on the substrate than the liquid that cools by in-flight convection, the dendrite arm spacing of the quenched liquid will be much smaller than the solid that forms in flight.

From Figures 4.4 (c) and 4.4 (d), it can be seen that the liquid in the droplet is quenched so fast that it is not allowed to flow down onto the substrate from the periphery of the droplet. The liquid on the periphery of the droplet explains why the surfaces of

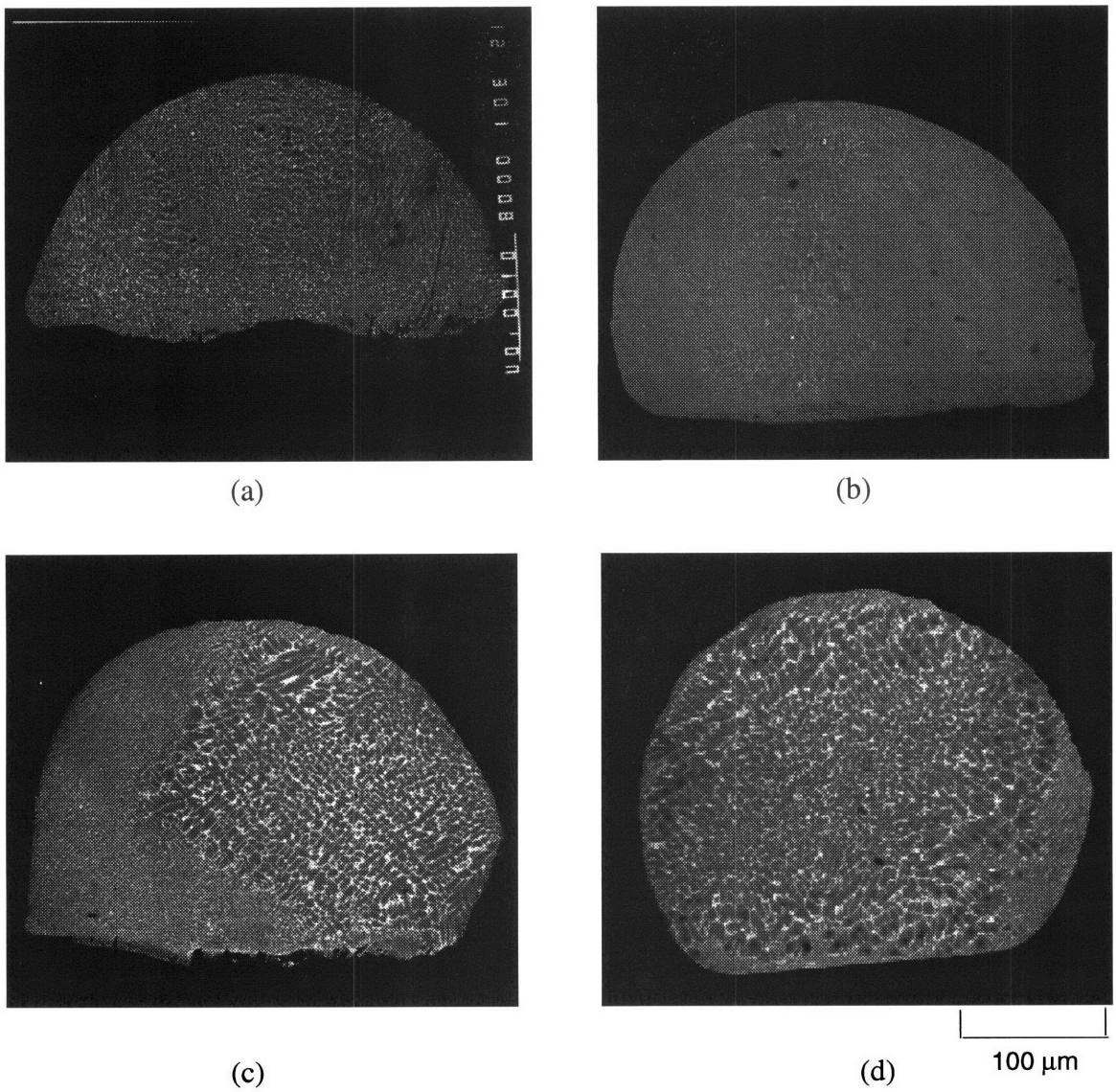

Figure 4.4 Micrographs of 295 µm, Al-4.5wt% Cu droplets quenched on metal substrates at (a) 0.4 m, (b) 0.42 m, (c) 0.46 m, and (d) 0.48 m away from the orifice.

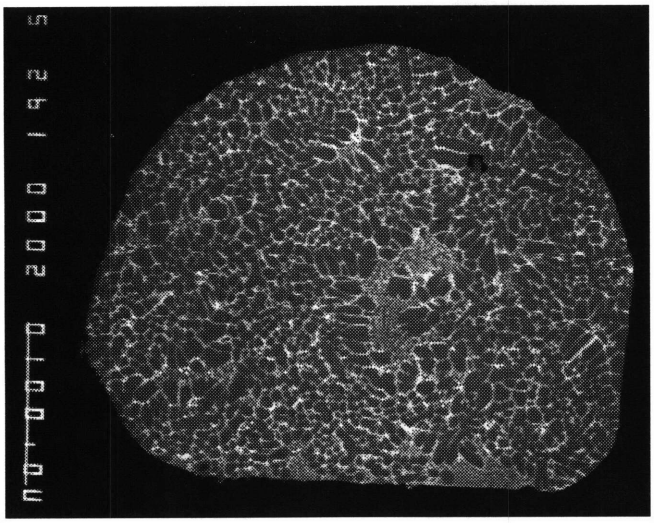

Figure 4.5 Micrograph of a 295 μm, Al-4.5wt% Cu droplet quenched at 0.48 m that shows internal liquid pockets.

rapidly solidified powders are uneven as it is due to solidification shrinkage. However, another splat collected at 0.48 m as shown in Figure 4.5, reveals that liquid can remain trapped inside the droplet during the later stages of flight.

From Figures 4.4 (c), (d), and 4.5, it is interesting to note how the microstructure of the quenched droplets exhibit progressively coarser structures outward from a point of nucleation. The dendrites adjacent to the liquid region are consistently the coarsest. The development of non-uniform solidification morphologies is usually associated with the effects of undercooling. The temperature of the solid-liquid interface increases as solidification progresses in droplets that experience undercooling [Sridharan and Perepezko 1994]. However, the degree of undercooling was probably slight since microstructures of the fully solidified powders are fairly uniform.

The solid fractions of the quenched droplets represented by the coarser dendritic regions are quantified from the micrographs with image analysis tools. The assumption that the ratio of the area covered by solid to the total cross-section area is equivalent to the volume fraction of solid in the droplet, is valid only if the microstructure is unbiased by the cross-section examined. By sectioning the samples into several parallel planes, it was discovered that the microstructure in Figure 4.4 (b) changes significantly, thereby causing the solid fraction measurement to be biased. Consequently, a more precise method is needed to measure the droplet solid fraction. Quenching the droplets in oil prevents deformation and allows the volume of solid to be estimated through different planes of observation.

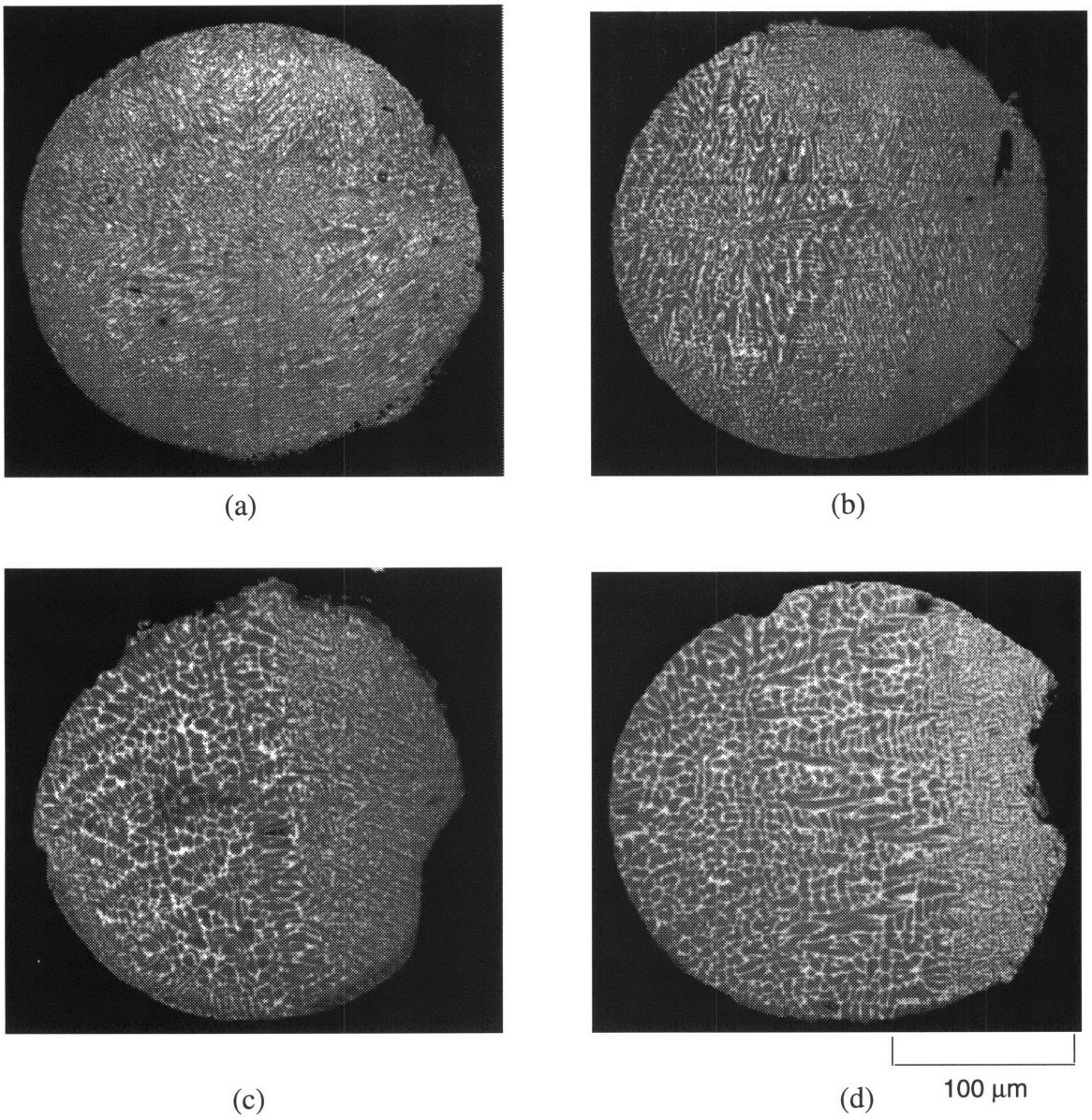

Figure 4.6 Micrographs of 275 μm, Al-4.5wt% Cu droplets quenched in oil at (a) 0.34 m, (b) 0.38 m, (c) 0.42 m, and (d) 0.46 m.

4.5.3 Oil-quenched Al-4.5wt% Cu droplets

Figures 4.6 (a) through (d) display the cross-sections of the droplets, with an average diameter of 275 μm, that were collected in oil cups at 0.34 m, 0.38 m, 0.42 m, and 0.46 m away from the orifice, respectively. The evolution of the droplet microstructure as flight distance increases is similar to that seen in the previous experiment except that the contrast

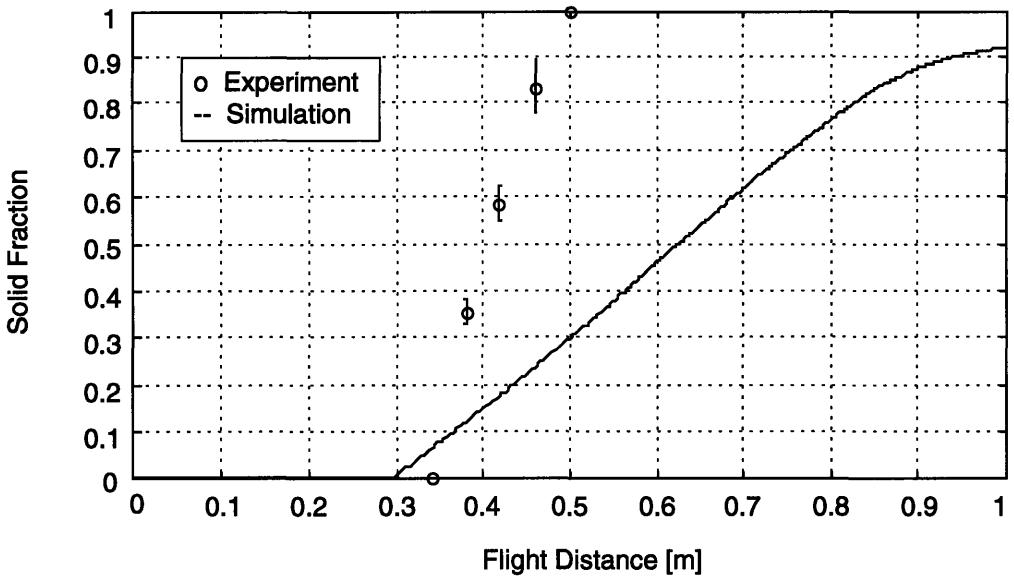

Figure 4.7 Simulation and experimental results for 275 μm droplet of Al-4.5wt% Cu.

between the different phases is less pronounced. Accordingly, quenching on a metal substrate has greater heat conduction path than quenching with an oil medium .

The oil-quenched samples were sectioned into several parallel planes to check for consistency of microstructure throughout the droplet volume. After each polishing sequence, micrographs are taken and the solid fraction is quantified. Unlike the substrate-quenched samples, the apparent solid fraction does not vary significantly from plane to plane. Therefore, a volume integration is unnecessary and the areal fraction can be assumed to approximate the volume fraction of the sample [Vandervoort 1984]. Using the same interpretation of the microstructure, the SEM results of the oil-quenched droplets are plotted against the simulation curve in Figure 4.7.

4.5.4 Al-4.3wt% Fe powders

The droplet quenching technique was performed with Al-4.3wt% Fe alloy to investigate the effect of composition on the definition of the solid formed in the droplets during flight. Two different microstructures were observed in Al-4.3wt% Fe powders, 250 μm in diameter, and are shown in Figures 4.8 (a) and (b). From a sampling of 7 powders, all of the powders exhibited microstructures similar to Figure 4.8 (a), except for one of the powders which is shown in Figure 4.8 (b). In Figure 4.8 (a), the microstructure is completely devoid of any well-defined dendritic or cellular structures. The homogeneity in the cross-sectional composition implies that the solutal Fe was not able to precipitate out of

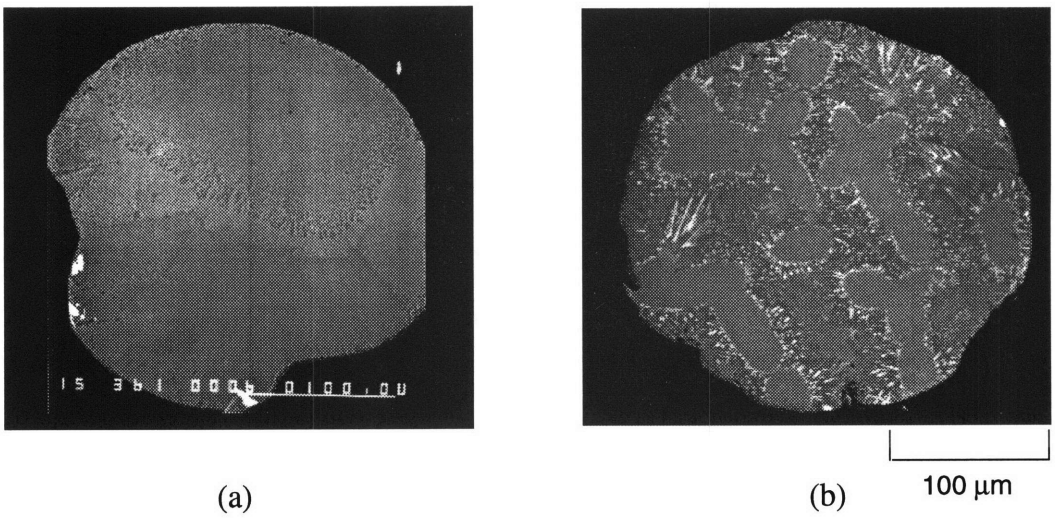

(a) (b)

Figure 4.8 Typical cross-sectional micrographs of 250 µm, Al-4.3wt% Fe powders collected at the bottom of the chamber, (a) completely undercooled and (b) partially undercooled.

the Al, even though Al has almost no solid solubility for Fe. It is evident that the Al-Fe droplets were completely undercooled in flight. Figure 4.8 (b) shows a variation of the undercooling phenomenon. Although the powder is of the same diameter, it appears to be only partially undercooled. In this case, the fine featureless region developed during the recalescence period following initial nucleation and external heat flow controlled the completion of solidification. To follow the progression of undercooling, the droplets are quenched at intermediate flight distances.

4.5.5 Substrate-quenched Al-4.3wt% Fe droplets

Figures 4.9 (a) through (d) show the cross-sections of the droplets with an average diameter of 250 µm, collected at 0.32 m, 0.36 m, 0.44 m, and 0.46 m away from the orifice, respectively. The microstructure evolution of the Al-Fe droplets during solidification is strikingly different than that seen in the Al-Cu droplets. It is particularly unusual that the droplets did not deform on impact with the substrates as the Al-Cu droplets did.

At the earlier flight distances, the microstructure is dominated by bright Fe-rich dendrites that streak across the droplet. In Figures 4.9 (a) and (b), however, there are also small regions of featureless structure that originate from the droplet surface. These featureless regions grow in size with increasing flight distance. With the Al-Cu droplets, it was reasoned that the fine crystalline structure observed early in flight is representative of

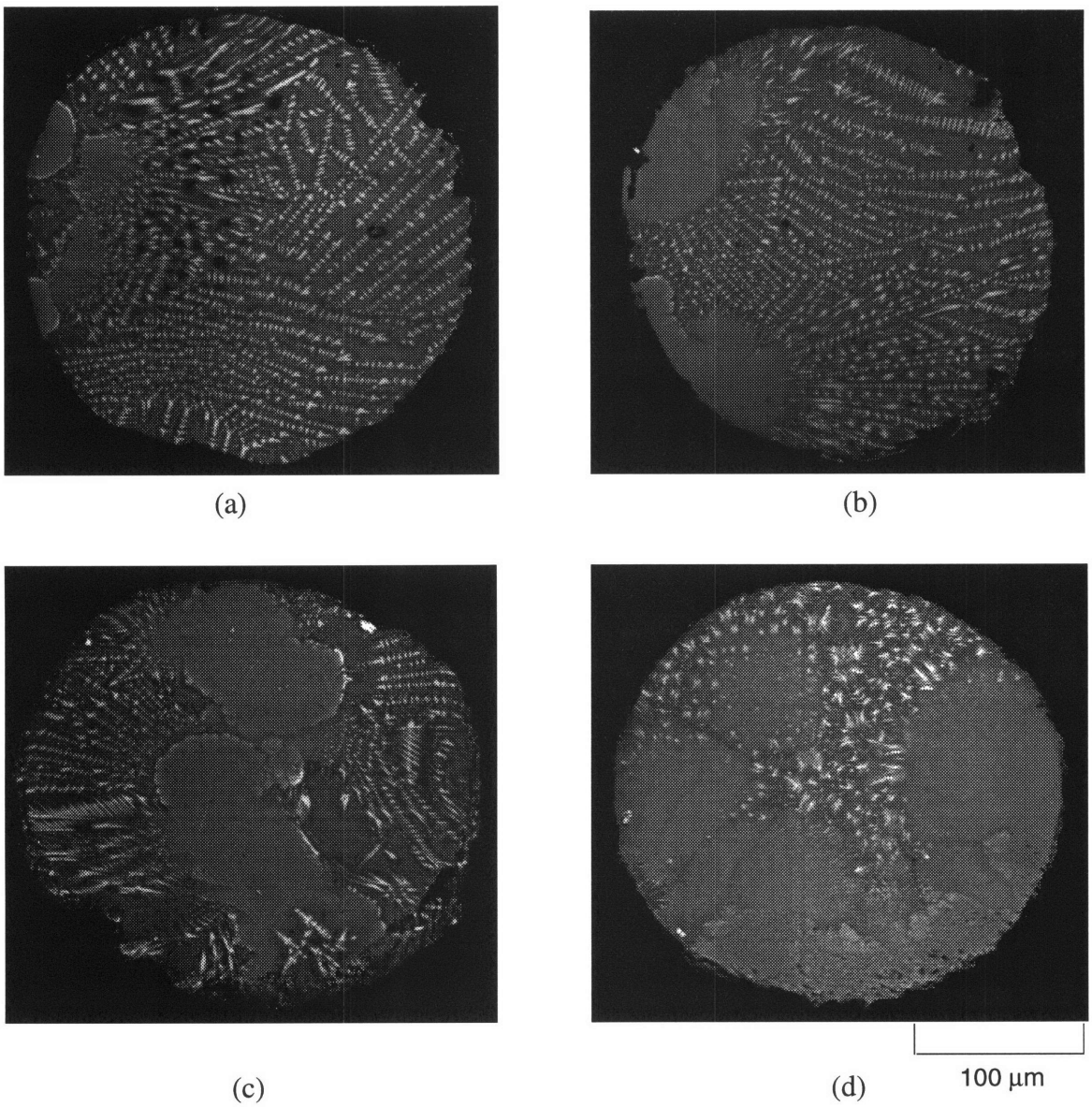

Figure 4.9 Micrographs of 250 μm Al-4.3wt% Fe droplets quenched on metal substrates at (a) 0.32 m, (b) 0.36 m, (c) 0.44 m, and (d) 0.46 m away from the orifice.

liquid quenched on impact with oil or a steel substrate. However, this is not the case with the Al-Fe droplets. As concluded from the microstructure of the Al-Fe powders, the featureless regions observed in the Al-Fe droplets must have formed during recalescence. The undercooling of the droplets collected during flight is interrupted by the impact with the substrates. When the droplet impacts the substrate, recalescence is instantaneously forced to occur in the undercooled regions. Without any contact area between the droplet and the substrate, the remaining liquid in the droplet solidifies at a much slower rate than the region that formed during recalescence, thereby producing a dendritic structure.

4.6 Discussion

4.6.1 Al-4.5wt% Cu droplets It is evident from Figure 4.7 that the validity of the solidification model based on Scheil's equation has not been substantiated. The experimental results for the Al-4.5wt% Cu droplets are consistently higher than the predicted values of droplet solid fraction during flight. The discrepancy implies that the coarse dendritic region observed in the quenched droplets is not fully solid, but rather that it is a mushy zone. However, it is not possible to determine what percentage of liquid still remains in the mushy zone.

Nonetheless, the temperature at which solid begins to form is in good agreement with the model. From the cross-sections of the quenched droplets, it can be inferred that the droplets probably experienced some undercooling since the dendrite arm spacing increases from a point of nucleation in the mushy zone. However, the uniform microstructure in the fully solidified power does not suggest that the undercooling is significant.

4.6.2 Dendrite arm spacing in Al-Cu microstructure

The secondary dendrite arm spacing (DAS) is measured in the Al-4.5wt% Cu powders to approximate of the cooling rate of the droplet in flight according to the empirically derived Equation (3.22) in Chapter 3. The average secondary DAS is 6.3 μm which should correspond to a cooling rate on the order of 500 Ks^{-1}. In contrast, the equilibrium droplet thermal model predicts a cooling rate on the order of 1900 Ks^{-1} and secondary DAS to be 4 μm. Consequently, microstructure of the fully solidified powders suggests that solidification could not have taken place faster than the thermal model predicts. Therefore, the microstructure of the quenched droplets were most likely interpreted incorrectly and lead to inflated values of solid fraction.

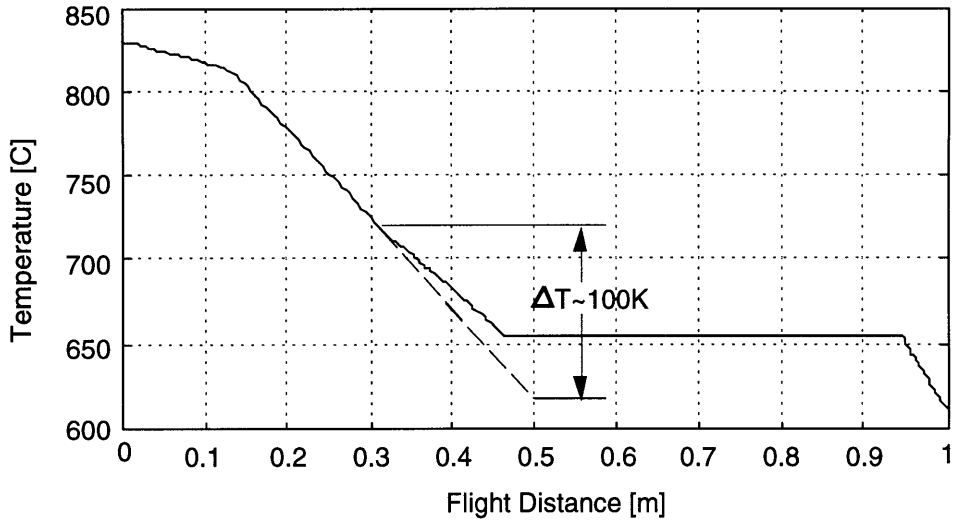

Figure 4.10 Estimated degree of undercooling for 250 μm Al-4.3wt% Fe droplets.

4.6.3 Al-4.3wt% Fe droplets

In the Al-Fe alloy situation, the model of equilibrium solidification is no longer appropriate to predict the droplet thermal state. However, the degree of undercooling can be estimated by extending the convective cooling region beyond the liquidus temperature of the alloy as shown in Figure 4.10. The difference between the liquidus temperature and the nucleation temperature is the amount of undercooling. Nucleation is assumed to occur just after 0.46 m in flight since the Al-Fe droplet collected at this distance appears to be almost completely undercooled. Therefore, a 250 μm droplet of Al-4.3wt% Fe can be undercooled as much as 100 K in the UDS process. According to other research literature, this amount of undercooling in such a large diameter droplet is quite unexpected [Rolland 1996, Chu 1996]. One reason for large undercooling may be the lack of violent conditions in the UDS process which are often encountered in conventional gas-atomized spray forming. The potential to produce novel microstructures with refined grain sizes is enhanced by the UDS process. Furthermore, this allows the production rate of the UDS process to be increased by using greater diameter orifices without sacrificing rapid solidification effects.

4.7 Advantages of Spraying with a Larger Orifice Diameter

Under conditions typical for gas-atomized spray forming of aluminum alloys, an exemplary powder size distribution is characterized by a mass mean powder diameter equal to 84 μm, with 84 cumulative weight percent of the distribution below 275 μm, and 16 cum.wt.%

below 23 μm [Lavernia et al 1992]. Traditionally, researchers have promoted spraying droplets with decreasing diameter since the higher cooling rates have been shown to increase the degree of microstructural refinement in the solidified powders. Specifically, much attention has been paid to understand how small droplets (<100 μm) can undercool [Sridharan and Perepezko 1994, Zhao 1992, Boettinger 1988, Perepezko et al 1986].

Undercooling is a solidification phenomenon that causes an alloy to nucleate below its liquidus temperature. At the nucleation temperature, a critical nuclei is formed and triggers part of the droplet to solidify in less than a millisecond during recalescence. The very rapid rate of recalescence has been shown to produce powder microstructures that are completely segregation free, significantly increase the solubility of alloying elements, and form metastable phases [Perepezko et al 1986]. However, the effect of droplet solidification in flight on the evolution of fine equiaxed microstructure in the sprayed deposit is not fully understood.

Researchers have also suggested that the development of equiaxed grain morphology during spray deposition is strongly influenced not only by the microstructure of the impinging droplet, but also by other mechanisms such as dendrite arm fragmentation and grain multiplication [Chen 1996, Annavarapu and Doherty 1993, Liang et al 1992, Lavernia et al 1992]. The deformation and fracture of dendrite arms inside mushy droplets occur when the incoming droplets impact the deposit surface. The fragmented dendrite arms act as growth centers of nucleation randomly oriented inside the deposit. The greater number of dendrite arms, the greater amount of grain multiplication which can lead to finer grain sizes. Therefore, it is possible that larger sized droplets can produce a fine equiaxed microstructure through dendrite arm fragmentation.

In addition to increasing the stream stability of liquid aluminum alloys in the UDS process, larger droplets allow the droplet solid fraction to be less sensitive to changes in flight distance. As a result, depositing droplets with a desired amount of solid can be more easily controlled. Furthermore, Chen [1996] showed in his studies with Zn-20wt% Sn, droplets in the UDS process experience higher undercooling than comparably sized droplets in conventional spray forming. Therefore, larger droplets may be used in the UDS process without compromising the goal of achieving fine equiaxed microstructure in the deposit for optimal mechanical properties.

Chapter 5 SUMMARY AND FUTURE WORK

5.1 Summary

Through the course of this work, the application of the UDS process to aluminum alloys was successfully accomplished by purifying the gas in the spray chamber to minimize oxygen and water vapor content. Initial attempts to spray aluminum alloys had produced erratic stream behavior. The oxidation of the molten aluminum stream as it exited from the crucible was interrupting the surface energy waves applied on the stream by piezoelectric vibration. With the implementation of a gas purification system described in Chapter 2, the uniform break-up of aluminum alloy jets from 150 and 200 μm diameter orifices was obtained with mass flow rates of approximately 0.25 and 0.43 g/sec, respectively.

In order to produce a deposit with optimal microstructure, it is important to characterize the thermal states of the droplets during flight. Newtonian cooling and the Scheil equation were employed together with the droplet trajectory model to predict the droplet temperature and solid fraction as a function of flight distance. The model was experimentally tested by quenching droplets of Al-4.5wt% Cu and Al-4.3wt% Fe alloys, respectively on metal substrates or in oil placed at different flight distances.

Based on metallographic examination of the quenched Al-Cu alloy droplets, the thermal model consistently underestimates the fraction of solid found in the droplets at a given flight distance. Two distinct regions of microstructure were observed in the droplets: a crystalline region with very fine dendrites and a coarser dendritic region. Due to the difference in cooling rates, the fine crystalline structure was interpreted as the liquid phase in the droplet before impact and the coarse dendrites as the solid phase. However, it is more likely that the coarse dendritic region is a mushy zone of solid and liquid phases rather than a fully solid phase during flight. This would explain why the solid fractions derived from image analysis are too high. Furthermore, the measurement of secondary dendrite arm spacing in powders collected after solidification confirmed that the cooling rate predicted by the thermal model is more realistic. In addition, the model assumption of complete convection in the liquid phase may also contribute to the deflation of predicted solid fraction values.

In efforts to avoid a mushy zone as the one found in the Al-4.5wt% Cu droplets, Al-4.3wt% Fe alloy droplets were tested. Fe has less than 0.06wt% solid solubility in Al. However, instead of undergoing equilibrium solidification, the Al-Fe powders exhibited a completely undercooled microstructure with no dendritic or cellular features. When the Al-Fe droplets were collected in flight, the droplets did not deform significantly on impact with metal substrates. Their microstructures showed regions of Fe-rich dendrites growing from

undercooled featureless regions. The featureless regions occupy more cross-sectional area with increasing flight distance. Therefore, the microstructure suggests that collecting the Al-Fe droplets in flight interrupts undercooling and forces recalescence to occur on impact, after which the remaining liquid portion cools at a slower rate and produces the dendrites. The Al-Fe droplets are estimated to undercool by 100 K. One reason for the large undercooling may be the lack of violent conditions in the UDS process which are often encountered in conventional gas-atomized spray forming.

In conclusion, the data obtained through the droplet quenching method do not substantiate the droplet thermal model for aluminum alloys. Further work is necessary to validate the model for cases with no undercooling of Al-Cu alloy droplets. The equilibrium solidification model is inappropriate for the 250 μm Al-Fe alloy droplets that were found to undercool completely within 0.50 m of flight distance. However, the Al-Fe alloy droplets offer the unique opportunity to produce novel deposit microstructures. Furthermore, this allows the production rate of the UDS process to be increased by using larger diameter orifices without sacrificing solidification effects.

5.2 Future Work

The long term goal in this project with aluminum alloys is to produce aluminum alloy sheets by using a multi-orifice UDS process. To accomplish this, the optimal processing conditions with respect to the droplet solid fraction and substrate temperature need to be established to produce full density, fine equiaxed deposit microstructure. A similar process-microstructure map for the UDS process has been established for tin-lead alloys by Chen et al [1996]. Although the data suggest that the droplet thermal model is adequate to predict droplet solid fraction in Al-4.5wt% Cu droplets, the droplet enthalpy measurement during flight needs to be made to further verify the model.

The tendency of Al-Fe alloy droplets to undercool in the UDS process opens many areas for further study. If the Al-Fe alloy droplets undercool during flight and are deposited on a substrate such that recalescence occurs on impact, then the effects of rapid solidification could be enhanced throughout the sprayed deposit. Because of rapid solidification rates during recalescence, the deposits would possess refined grain sizes, high levels of solid solubility, and very limited phase segregation. However, if the undercooling phenomenon proved difficult to control, then the droplet size should be increased significantly to avoid undercooling while simultaneously increasing the production rate of the UDS process. Therefore, future work will consist of the following sequence of tasks:

(1) Measure the droplet enthalpy of Al-4.5wt% Cu and Al-4.3wt% Fe alloy droplets using a non-adiabatic calorimeter.
(2) Develop a process-microstructure map to correlate the processing parameters for Al alloys to deposit microstructure.
(3) Spray form flat sheets of Al-alloy using multiple orifices.
(4) Rapid prototype 3-dimensional parts.

Bibliography

Abel, G.K., 1993, "Design and Contruction of High Temperature Uniform Metal Spray Apparatus," SB Thesis, Mechanical Engineering, MIT.

Abel, G.K., 1994, "Characterization of Droplet Flight Path and Mass Flux in Droplet-Based Manufacturing," SM Thesis, Mechanical Engineering, MIT.

Annavarapu, S. and Doherty, R.D., 1993, "Evolution of Microstructure in Spray Casting," International Journal of Powder Metallurgy, vol 29 no 4, pp 331-343.

Aubrey, L.S. and Dore, J.E., 1993, "Ceramic Foam - A Deep Bed or Caking Filter in Aluminum Cast Shop Operations," Light Metals, The MM&M Society, pp 1009-1020.

Bewlay, B.P. and Cantor, B., 1990, Metallurgical Transactions, 21B, p 899.

Boettinger, W.J., 1988, "Microstructural Variations in Rapidly Solidified Alloys," Materials Science and Engineering, vol 98, pp 123-130.

Chen, C.-A., 1996, "Droplet Solidification and its Effects on Deposit Microstructure in the Uniform Droplet Spray Process," Ph.D. Thesis, Mechanical Engineering, MIT.

Chen, C.-A., Acquaviva, P.J., Chun, J.-H., and Ando, T., 1996, "Effects of Droplet Thermal State on Deposit Microstructure in Spray Forming," Scripta Materialia, vol 34, no 5, pp 689-696

Chu, M.G., 1996, Aluminum Company of America, personal phone conversation.

Cotton, J.D. and Kaufman, M.J., 1991, "Microstructural Evolution in Rapidly Solidified Al-Fe Alloys," Metallurgical Transactions A, vol 22A, pp 927-934.

Flemings, M.C., 1974, "Solidification Processing," McGraw-Hill.

Grant, P.S. and Cantor, B., 1995, "Modelling of Droplet Dynamic and Thermal Histories during Spray Forming - III", Acta Metall. Mater., vol 43, no 3, pp 913-921.

Hultgren, R., Desai, P., Hawkins, D., Gleiser, M., and Kelley, K., 1973, "Selected Values of the Thermodynamic Properties of the Elements," ASM.

Kim, H.-Y., 1996, "Microsensor Development for the Study of Droplet Spreading," SM Thesis, Mechanical Engineering, MIT.

Kubaschewski, O. and Alcock, C.B., 1979, "Metallurgical Thermochemistry," Pergamon Press, 5th ed.

Lavernia, E.J., Ayers, J.d., and Srivatsan, T.S., 1992, "Rapid Solidification Processing with Specific Application to Aluminum Alloys," International Materials Review, vol 37, pp 1-44.

Leatham, A., 1996, "Spray Forming Technology," Advanced Materials & Processes, vol 150 no 2, pp 31-33.

Lee, E.S. and Ahn, S., 1994, "Solidification Progress and Heat Transfer Analysis of Gas-Stomized Alloy Droplets During Spray Forming," Acta Metall. Mater., vol 42, no 9, pp 3231-3243.

Leon, D.D. and Kozarek, R.L., 1995, "Use and Characterization of Linear Nozzles for Spray Forming," Advances in Powder Metall. and Particulate Mater. Proceedings, Intnl. Conf. & Exhibt. on Powder Metall. & Particulate Mater, Part 2 of 3.

Liang, X., Earthman, J.C., and Lavernia, E.J., 1992, "On the Mechanism of Grain Formation During Spray Atomization and Deposition," Acta Metall. Mater., vol 40, no 11, pp 3003-3016.

Lu, S.Z., Hunt, J.D., Gilgien, P., and Kurz, W.,1994, "Cellular and Dendritic Growth in Rapidly Solidified Al-Fe and Al-Cu Alloys," Acta Metall. Mater. vol 42, no 5, pp 1653-1660.

Mathur, P., Annavarapu, S., Apelian, D., and Lawley, A., 1991, "Spray casting: an integral model for process understanding and control," Materials Sci & Eng A, vol A142, pp 261-276.

Mulholland, J.A., Srivastava, R.K. and J.O.L. Wendt, 1988, "Influence of Droplet Spacing on Drag Coefficient in Nonevaporating, Monodisperse Streams," AIAA Journal, vol 25 no 10, pp 1231-1237.

Nylund, A. and Olefjord, I., 1991, "Surface Analysis of USGA Aluminum and Aluminum Alloy Powders," Materials Science & Engineering A, vol A134, pp 1139-1143.

Passow, C.H., 1992, "A Study of Spray Forming Using Uniform Droplet Sprays," SM Thesis, Mechanical Engineering, MIT.

Perepezko, J., LeBeau, S., Mueller, B. and Hildeman, G., 1986, "Rapid Solidification of Highly Undercooled Aluminum Powders," ASTM STP 890, pp 118-136.

Ragone, D.V., 1995, "Thermodynamics of Materials," John Wiley & Sons.

Rayleigh, Lord, On the Instability of Jets, 1878, Proceedings of London Mathematical Society, vol 10, pp 4-13

Rolland, M., 1994, "Spray Forming, Droplet Microstructure and Impingement Behavior," SM Thesis, Materials Science and Engineering, MIT.

Sahu, S., 1994, "Thermal State of Sn-Pb Droplets in the Droplet-Based Manufacturing Process," SM Thesis, Mechanical Engineering, MIT.

Brandes, E.A. and Brook, G.B., 1992, "Smithells Metals Reference Book," 7th ed. Butterworth-Heineman Ltd.

Sridharan, K. and Perepezko, J.H., 1994, "Microstructural Control in Alloy Steel Powders," International Journal of Powder Metallurgy, vol 30, no 3, pp 301-311.

Stone, I.C. and Tsakiropoulos, P. "Cooling Rates in Gas Atomised Al-4.5wt% Alloy Powders," International J. Rapid Solidification, 1992, vol 7, pp 177-190

Tsao, C.-Y. and Grant, N.J., 1994, "Modeling of the Liquid Dynamic Compaction Spray Process," International Journal of Powder Metallurgy, vol 30 no 3, pp 323-333.

Tyler, D.E. and Watson, W.G., 1996, "Nucleated Casting," Proc. 3rd Intl Spray Forming Conference, Cardiff, Wales.

Underhill, R.P., Grant, P.S., and Cantor, B., 1993, "Microstructure of Spray-Formed Al Alloy 2618," Materials & Design, vol 14 no 1, pp 45-47.

VanderVoort, G., 1984, "Metallography Principles and Practice," McGraw-Hill, p 425.

Yim, P., 1996, "The Role of Surface Oxidation in the Break-Up of Laminar Liquid Metal Jets," Ph.D. Thesis, Mechanical Engineering, MIT

Zhao, Q., 1992, "Evolution of the Rapid Solidification Structure of Highly Undercooled Ni-25wt% Sn Alloy," Ph.D. Thesis, Materials Science and Engineering, MIT.

Appendix A MATLAB Simulation Code

```
%% Declare Variables and Initial Values
%%%%%%%%%%%%%%%%%
% Gravitational Acceleration [m/s2]
     g = 9.81;
% Permittivity of Free Space [C2/Mm2]
        ezero = 8.85e-12;

% Gas Properties for Argon %% Gas #2
%%%%%%%%%%%%%%%%%
% gas density [kg/m3] (@300K 1990-91 CRC 6-17)
        Dg(2) = 1.623;
% gas viscosity [Ns/m2] (@300K 1990-91 CRC 6-17)
        Vg(2) = 2.27E-5;
% gas conductivity [W/mK] (@300K 1990-91 CRC 6-17)
        Kg(2) = 1.77E-2;
% chosen gas (argon)
        gas = 2;

% Properties for Al-Cu alloy
%%%%%%%%%%%%%%%%%
% weight percentage of Cu
        Co=0.045;
        Cl=0.045;
        Cs=0;
%initial melt temperature (deg C)
        T=750;
%density of the alloy [kg/m3]
        fl=0;
        density=dAlCu(Co,Cl,Cs,fl,T);
%liquidus temperature [deg C]
        atmCl=100*Cl/(2.355-1.355*Cl);
        Tl=660.6-5.37*atmCl-0.3437*atmCl^2
          +0.04315*atmCl^3-2.205e-3*atmCl^4+3.716e-5*atmCl^5;
%initial melt enthalpy [J/kg]
        en=eAlCulqd(Co,T);

% Control Parameters
%%%%%%%%%%%%%%%%%
% orifice diameter [m]
        orifice = 155E-6;
% driving pressure [psi]
        pressure = 9.75;
% driving frequency [Hz]
        frq = 7330;
% charger diameter [m]
        charger_diameter = 0.0045;
% charger voltage [volts]
        charger_voltage = 650;
% measured mass flow rate [kg/sec]
        mflow = 2.2e-4;
```

```
        gas_temperature = 40;
        substrate_position = 1.0

% Jet Parameters
%%%%%%%%%%%%%%%%
% volume flow rate
        vflow = mflow/density;
% jet diameter [m]
        dj = orifice;
% jet velocity [m/s] (+downward)
        vj = vflow/(pi*(dj^2)/4);
% exit coefficient
        dc = .82;

% Droplet Parameters
%%%%%%%%%%%%%%%%%%
% droplet diameter [m]
        %d = ((6/4)*dj^2*vj/frq)^(1/3)
        d = 275e-6;
% droplet cross sectional area [m2]
        ac = (1/4)*pi*d^2;
% droplet surface area [m2]
        as = pi*d^2;
% droplet volume [m3]
        vlm = (1/6)*pi*d^3;
% droplet mass [kg]
        density;
        m = density*vlm;
% charger capacitance [farads] (check this d should be orifice diameter)
        charger_capacitance = 2*pi*ezero*(vj/frq)/log(charger_diameter/dj);
% droplet charge [Coulombs]
        q = charger_capacitance*charger_voltage;
% scatter constant
        sc = q*q/((4*pi*ezero)*((1/6)*pi*d^3*density));

% Counting Parameters
%%%%%%%%%%%%%%%%
% number of droplets for spreading calculations
        nd = 20;
% time per spreading step
        tpss = 0.0001;
% number of spreading steps per flight step
        nsspfs = 10;
% time per flight step
        tpfs = nsspfs*tpss;
% number of steps (approximate)
        ns = abs(round(substrate_position/(vj*tpfs)));
% number of data points (approxiamte)
        ndp = 50;
% number of steps per data point
        nspdp = ceil(ns/ndp);

% Droplet Initial Conditions and Data Variables
%%%%%%%%%%%%%%%%
```

```
% initial compostion increment
        dCl = 0.0001;
% initial temperature increment
        dT=0.35;        % 275 micron droplet
        %dT=0.15;     % 400 micron droplet
% initial solid fraction
        fs = 0;
        fs_eut = 0;
% position [m] (measured from orifice (+z downward)
        xc = 0.0001*d*rand(nd,1);
        for j=1:nd
          xc(j) = xc(j)+(0.00001*d*cos(pi*j));
        end
        yc = 0.0001*d*rand(nd,1);
        zcur = 0;
        x = zeros(ndp,1);
        y = zeros(ndp,1);
        z = zeros(ndp,1);
% velocity [m/s] (+vz downward)
        vxc = zeros(nd,1);
        vyc = zeros(nd,1);
        vzcur = vj;
        vx = zeros(ndp,1);
        vy = zeros(ndp,1);
        vz = zeros(ndp,1);
% accelerations [m/s2] (+az downward)
        axc = zeros(nd,1);
        ayc = zeros(nd,1);
        azcur = 0;
        ax = zeros(ndp,1);
        ay = zeros(ndp,1);
        az = zeros(ndp,1);
% thermal data variables
        sT(1)=T;
        sflqd(1)=1;
        sv(1)=vzcur;
        sz(1)=0;
        stime(1)=0;
        sCl(1)=Cl;
        sen(1)=en;

% Intermediate Variables
%%%%%%%%%%%%
% Counters n(step), dc(data), i,j,k(misc)
% Reynold's Number Re
% Prandlt Number Pr
% Drag Coefficient from Mathur and Gutierrez-Miravete et. al. Cdm
% Drag Coefficients from Mulholland, Srivastava, and Wendt:
%   for a single droplet Cd_inf
%   for a rod Cd_rod
%   for a stream of droplets approximating a rod Cd_one
%   for a stream of droplets Cd_stream
%   combined drag coefficient Cd_combined
% Heat Transfer Coefficient h
```

```
% Rate of Heat Transfer Q
% Number of Droplets in Currently in Flight nfd

%%%%%%%%%%%%
% The Simulation
%%%%%%%%%%%%
n = 1;
dc = 1;

while zcur<substrate_position
n = n+1;

% Calculate Vertical Droplet Acceleration
%%%%%%%%%%%%
Re = abs(vzcur*d*Dg(gas)/Vg(gas));
clearance = sqrt(xc(1)^2+yc(1)^2);
Cdm = 0.28+(6/(Re^0.5))+(21/Re);

if clearance>d
  aznew = g-(Cdm*Dg(gas)*(vzcur^2)*ac)/(2*m);
else
  Cd_inf = Cdm;
  Cd_rod = 0.755/Re;
  Cd_one = (Cd_rod^(-0.678)-Cd_inf^(-0.678))^(-1/0.678);
  Cd_one_plus = Cd_one+(43/Re)*(((vzcur/frq)/d)-1);
  Cd_stream = (Cd_one_plus^(-0.678)+Cd_inf^(-0.678))^(-1/0.678);
  Cd_combined =((d-clearance)/d)*Cd_stream+(clearance/d)*Cd_inf;
  aznew = g-(Cd_combined*Dg(gas)*(vzcur^2)*ac)/(2*m);
end

% Calculate Droplet Thermal State
%%%%%%%%%%%%
if zcur < 0.8
 gas_temperature = 143.7*zcur^2 - 220*zcur + 108.5;
else
 gas_temperature = 26;
end

Cg = specheat(gas,gas_temperature);
avgtmp = (gas_temperature+T)/2;
Cga = specheat(gas,avgtmp);
Re = abs(vzcur*d*Dg(gas)/Vg(gas));
Pr = Vg(gas)*Cg/Kg(gas);
h = Kg(gas)*(2+0.6*(Re^0.5)*(Pr^0.33))*((Cga/Cg)^0.26)/d
if clearance<d
  zspry=zcur;
  h = h*(Cd_combined/Cd_inf)
end

Q=h*tpfs*as*(T-gas_temperature)/m          % per unit mass

% Calculate thermal variables and density change
%%%%%%%%%%%%
if T>Tl
```

```
 [T,dT]=fAlCulqd(Q,en,Co,T,dT)
 fl=1;
 en=en-Q;
 if T<Tl        % This "if" loop is put here to avoid temperature jump at Tl
  T=Tl;
 end
else
 if fl>0
   en
   [Cl,Cs,Tk,fs,dCl]=fAlCumushy(Q,en,Cl,fs,dCl)
   T=Tk-273;
   fl=1-fs;
   en=en-Q;
 else
   fl=0;
   T=fAlCusld(Q,en,Co,T);
   en=en-Q;
 end
end

% Calculate Droplet Surface Area
%%%%%%%%%%%%%
density=dAlCu(Co,Cl,Cs,fl,T);
vlm=m/density;
d=(6*vlm/pi)^(1/3);
as=pi*d^2;

% Calculate Droplet Scattering
%%%%%%%%%%%%%
if sqrt(xc(nd)^2+yc(nd)^2)<(5*d)
  step = nsspfs;
  period = tpss;
else
  step = 1;
  period = tpfs;
end
nfd=nd;
for i = 1:step
  for j = 1:nfd
    axn(j) = 0;
    ayn(j) = 0;
    for k = 1:nfd
        if k ~= j
           dnm = (xc(j)-xc(k))^2+(yc(j)-yc(k))^2+((j-k)*(vzcur/frq))^2;
           axn(j) = axn(j)+sc*(xc(j)-xc(k))/dnm^(3/2);
           ayn(j) = ayn(j)+sc*(yc(j)-yc(k))/dnm^(3/2);
    end
   end
end
  for j = 1:nfd
    vxn(j) = vxc(j)+((axn(j)+axc(j))/2)*(period);
    vyn(j) = vyc(j)+((ayn(j)+ayc(j))/2)*(period);
    axc(j) = axn(j);
    ayc(j) = ayn(j);
```

```
    xc(j) = xc(j)+((vxn(j)+vxc(j))/2)*(period);
    yc(j) = yc(j)+((vyn(j)+vyc(j))/2)*(period);
    vxc(j) = vxn(j);
    vyc(j) = vyn(j);
  end
end

% Update Variables
%%%%%%%%%%%%
vznew = vzcur+((aznew+azcur)/2)*tpfs;
azcur = aznew;
zcur = zcur+((vznew+vzcur)/2)*tpfs;
vzcur = vznew;

% store data
%%%%%%%%%%%%
sT(n)=T;
sflqd(n)=fl;
sv(n)=vzcur;
sz(n)=zcur;
stime(n)=(n-1)*tpfs;
sCl(n)=Cl;
end  % while loop
save zno100 sT sflqd sv sz stime tpfs zspry;


%%%%%%%%
function D=DAlCu(Co,Cl,Cs,fl,T)

atmCo=100*Co/(2.355-1.355*Co);
Tl=660.6-5.37*atmCo-0.3437*atmCo^2+0.04315*atmCo^3-2.205e-3*atmCo^4;
                                          % Tl in deg C

DCus=8960;                                %density in kg/m^3
DCul=8867-0.801*T;
DAls=2700;
DAll=2570-0.280*T;
if T > Tl
    D=1/((1-Co)/DAll+Co/DCul);
else
    if T>= 571
        fs=1-fl;
        D= 1/((fl*(1-Cl)/DAll)+(fl*Cl/DCul)+(fs*(1-Cs)/DAls)+(fs*Cs/DCus));
    else
        D=1/((1-Co)/DAls+Co/DCus);
    end
end
end

%%%%%%%%
function [T, dT]=fAlCulqd(den,olden,Co,oldT,dT)

T=oldT-dT;                                % decrease T, solve for new en.
```

```
en=eAlCulqd(Co,T);                    % check to see if new en - old en = Q
endiff=olden-en;
while (abs((den-endiff)/den) > 0.01)  % keep decreasing T until it does
 if den>endiff
   T=T-0.001;
   en=eAlCulqd(Co,T);
   endiff=olden-en;
 else
   T=T+0.001;
   en=eAlCulqd(Co,T);
   endiff=olden-en;
 end
end
dT=oldT-T;
end


%%%%%%%%
function en=eAlCulqd(Co,T)

Tk=T+273.15;
eAll=(7.59*Tk-204)*4.184*1000/26.98;
eCul=(7.8*Tk-284)*4.184*1000/63.54;
en=(1-Co)*eAll+Co*eCul;%unit for enthalpy is j/kg
end


%%%%%%%%
function [T,Cs]=mushy(Cl)

atmCl=100*Co/(2.355-1.355*Co);        %change from wt to atomic %
T=660.6-5.37*atmCl-0.3437*atmCl^2+0.04315*atmCl^3-2.205e-3*atmCl^4;
Cs=(-0.0506*T+33.4)/100;              %Cs as a fcn of T, solidus curve
end


%%%%%%%%
function
   [newCl,newCs,newTk,fs,newdCl]=fAlCumushy(den,olden,oldCl,oldfs,dCl)

[oldTk,oldCs] = mushy(oldCl)          %current Cs and T at current Cl
fs_dif = dCl*(1-oldfs)/(oldCl-oldCs);%increase in fs due to increase in Cl
fs = oldfs + fs_dif;                  %new fs

[newTk,newCs] = mushy(newCl)          %new Cs and T at new Cl
en=eAlCumushy(newCs,newCl,newTk,fs); %calculate new droplet enthalpy
endiff=olden-en                       %loss in enthalpy should equal Q!
newdCl=newCl-oldCl;

while (abs((den-endiff)/den) > 0.01)  %loop to find the correct new temp
 if den>endiff
   dCl = dCl + 0.00001;
   fs_dif = dCl*(1-oldfs)/(oldCl-oldCs);  %recalculate associated change in fs
   fs = oldfs + fs_dif
```

```
  newCl = oldCl + dCl;                    %change Cl,Tk, and Cs acccordingly
  [newTk,newCs] = mushy(newCl)
  en=eAlCumushy(newCs,newCl,newTk,fs);
  endiff=olden-en
  newdCl=newCl-oldCl;
  if den<endiff
   while (abs((den-endiff)/den) > 0.01)
    dCl = dCl - 0.0000005;
    fs_dif = dCl*(1-oldfs)/(oldCl-oldCs);
    fs = oldfs + fs_dif;
    newCl = oldCl + dCl;
    [newTk,newCs] = mushy(newCl)
   en=eAlCumushy(newCs,newCl,newTk,fs);
   endiff=olden-en
   newdCl=newCl-oldCl;
  end
  end
 else
  dCl = dCl - 0.00001;
  fs_dif = dCl*(1-oldfs)/(oldCl-oldCs);   %recalculate associated change in fs
  fs = oldfs + fs_dif
  newCl = oldCl + dCl;                    %change Cl,Tk, and Cs acccordingly
  [newTk,newCs] = mushy(newCl)
  en=AlCumushy(newCs,newCl,newTk,fs);
  endiff=olden-en
  newdCl=newCl-oldCl;
  if den>endiff
   while (abs((den-endiff)/den) > 0.01)
    dCl = dCl + 0.0000005;
    fs_dif = dCl*(1-oldfs)/(oldCl-oldCs);
    fs = oldfs + fs_dif;
    newCl = oldCl + dCl;
    [newTk,newCs] = mushy(newCl)
    en=eAlCumushy(newCs,newCl,newTk,fs);
    endiff=olden-en
    newdCl=newCl-oldCl;
   end
  end
 end
end


%%%%%%%%
function total=eAlCumushy(Cs,Cl,Tk,fs)

Co=0.045;
Cs_avg = (Co-Cl*(1-fs))/fs;
eAls=(6.8*Tk-2124)*4.184*1000/26.98;          % in j/kg
eAll=(7.59*Tk-204)*4.184*1000/26.98;
eCul=(7.8*Tk-284)*4.184*1000/63.54;
eCus=(6.7*Tk-2125)*4.184*1000/63.54;
fl=1-fs;
total=fs*(1-Cs_avg)*eAls+fs*Cs_avg*eCus+fl*(1-Cl)*eAll+fl*Cl*eCul;
end
```

```
%%%%%%%%
function T=fAlCusld(den,olden,Co,oldT)

T=oldT-0.0005
en=eAlCusld(Co,T)
endiff=olden-en
while (abs((den-endiff)/den) > 0.1)
 if den>endiff
   T=T-0.001
   en=eAlCusld(Co,T)
   endiff=olden-en
 else
   T=T+0.001
   en=eAlCusld(Co,T)
   endiff=olden-en
 end
end


%%%%%%%%
function en=eAlCusld(Co,T)

Tk=T+273.15;
eAls=(6.8*Tk-2124)*4.184*1000/26.98;          %unit for enthalpy is j/kg
eCus=(6.7*Tk-2125)*4.184*1000/63.54;
en=(1-Co)*eAls+Co*eCus;
end
```

Appendix B Thermophysical Properties of Al-Cu and Al-Fe alloys

The densities for pure Al, Cu, and Fe in solid and liquid states are expressed in kg/m^3 as [Brandes and Brooks 1992]:

$$
\begin{aligned}
D_{s,Al} &= 2700 \\
D_{l,Al} &= 2646 - 0.280 \times T \\
D_{s,Cu} &= 8960 \\
D_{l,Cu} &= 9086 - 0.801 \times T \\
D_{s,Fe} &= 7870 \\
D_{l,Fe} &= 8598 - 0.833 \times T
\end{aligned}
$$

where T is the temperature in degrees K. .

The enthalpies for pure Al, Cu, and Fe in solid and liquid states are expressed with respect to the standard state as [Hultgren et al 1973]:

$$
\begin{aligned}
H_{s,Al} - H_{ST} &= 1.055 \times T - 329.4 \\
H_{l,Al} - H_{ST} &= 7.59 \times T - 31.64 \\
H_{s,Cu} - H_{ST} &= 0.4412 \times T - 139.9 \\
H_{l,Cu} - H_{ST} &= 0.5136 \times T - 18.70 \\
H_{s,Fe} - H_{ST} &= 3.896 \times 10^{-4} \times T^2 + 0.1224 \times T - 66.25 \\
H_{l,Fe} - H_{ST} &= 1.498 \times 10^{-5} \times T^2 + 0.7327 \times T - 52.29
\end{aligned}
$$

The unit for enthalpy is kJ/kg and the temperature is in degrees K.

The phase diagrams for the Al-Cu and Al-Fe binary alloy systems are given in Figures A.1 and A.2, respectively. The polynomial expression for the equilibrium liquidus temperature of hypoeutectic Al-Cu alloys was taken to be [Lu et al 1994]:

$$
\begin{aligned}
T_{l,Al-Cu} = 933.6 &- 7.291 C_{Cu} + 0.3067 C_{Cu}^{\,2} \\
&- 7.033 \times 10^{-2} C_{Cu}^{\,3} + 2.802 \times 10^{-3} C_{Cu}^{\,4} \\
&- 4.362 \times 10^{-5} C_{Cu}^{\,5}
\end{aligned}
$$

where $T_{l,Al-Cu}$ is the liquidus temperature in K and C_{Cu} is the atomic percent of Cu in the alloy.

The expression for the equilibrium solidus temperature of hypoeutectic Al-Cu alloys was fitted by linear regression to be:

$$C_{Cu} = -0.0506 \times (T_{s,Al-Cu} - 273) + 33.4$$

where $T_{s,Al-Cu}$ is the solidus temperature in K and C_{Cu} is the weight percent of Cu.

The polynomial expression for the equilibrium liquidus temperature of hypereutectic Al-Fe alloys was fitted to be:

$$T_{l,Al-Fe} = 0.0015 \times C_{Fe}^{3} - 0.451 \times C_{Fe}^{2} + 29.69 \times C_{Fe} + 864$$

where $T_{l,Al-Fe}$ is the liquidus temperature in K and C_{Fe} is the weight percent of Fe in the alloy. The equilibrium solidus concentration of Fe is approximately constant at 36.5wt% Fe for all temperatures between 1420 K and the eutectic temperature at 928 K.

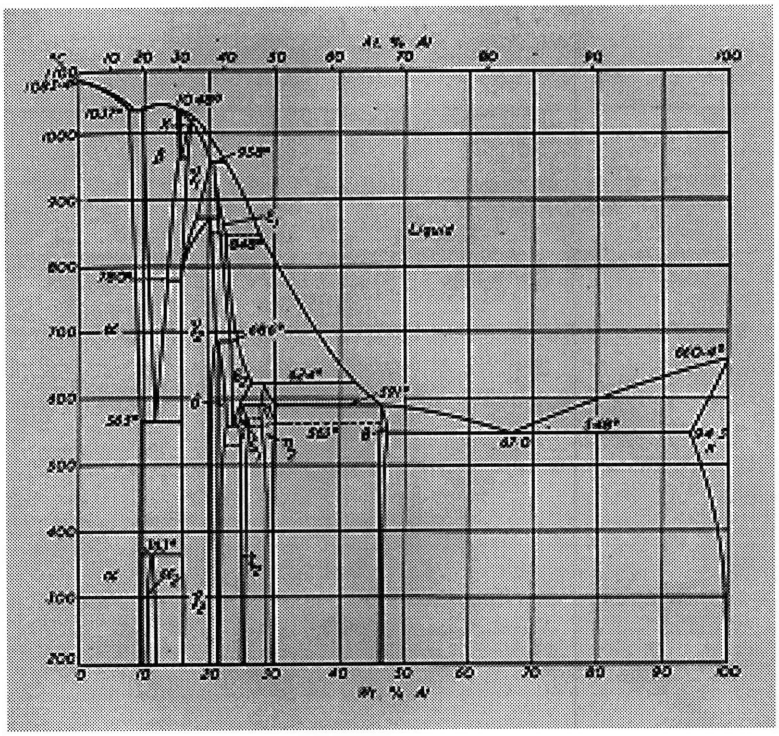

Figure A.1 Al-Cu phase diagram.

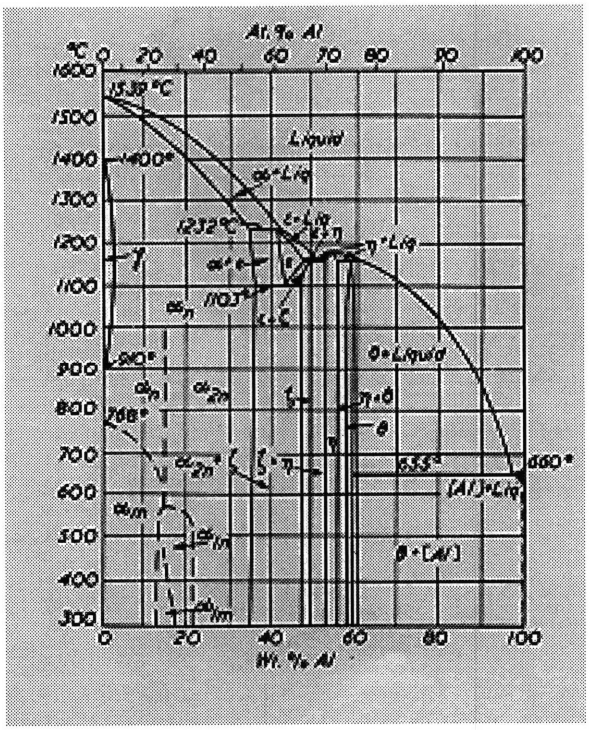

Figure A.2 Al-Fe phase diagram